Yu Ito[1]
Mem. ASME
Associate Professor
Department of Aeronautics and Astronautics,
The University of Tokyo,
7-3-1 Hongo, Bunkyo-ku,
Tokyo 113-8656, Japan
e-mail: itoyu110@00.alumni.u-tokyo.ac.jp

Toshinori Watanabe
Professor
Department of Aeronautics and Astronautics,
The University of Tokyo,
7-3-1 Hongo, Bunkyo-ku,
Tokyo 113-8656, Japan

Naoki Seki
Engine Technology Department,
IHI Corporation,
3975-18 Hajima-cho, Akishima,
Tokyo 196-8686, Japan

Karin Hirakawa
Engine Technology Department,
IHI Corporation,
3975-18 Hajima-cho, Akishima,
Tokyo 196-8686, Japan

Tomoya Inoue
Civil Engine Engineering Department,
IHI Corporation,
3975-18 Hajima-cho, Akishima,
Tokyo 196-8686, Japan

Takehiro Himeno
Professor
Department of Aeronautics and Astronautics,
The University of Tokyo,
7-3-1 Hongo, Bunkyo-ku,
Tokyo 113-8656, Japan

Effect of Channel Size on Air-Cooling Performance in Interior Permanent Magnet Motor Driving Aviation Fans at High Altitude

To enhance worldwide environmental conditions, the air transport industry must drastically reduce carbon dioxide emissions. Electrification of aircraft propulsion systems is one way to meet this demand. In particular, the focus is on obtaining single-aisle aircraft with partial turbo-electric propulsion and approximately 150 passenger seats by the 2030s. To develop a single-aisle aircraft with partial turbo-electric propulsion, an air-cooled interior permanent magnet (IPM) motor with an output of 2 MW is desired. One of the most difficult problems in air cooling is that air-cooling performance decreases with increasing altitude because the air density decreases. To investigate the effect of altitude on air-cooling performance in the IPM motor, the authors formulated mathematical system equations to describe heat transfer inside the target air-cooled IPM motor, and mathematical analytical solutions were obtained. The most severe condition is the top-of-climb condition. For this condition, a designer should choose cooling air mass flow rates that keep the temperature of the permanent magnets below the maximum temperature limit of 100 °C and the temperature of the coils below the maximum temperature limit of 250 °C. Here, the sizes of the air-cooling channels strongly affect air cooling with the IPM motor. In this paper, the authors briefly review the mathematical formulations and their solutions, investigate the effect of channel size on air-cooling performance in an IPM motor, and explore the optimum configuration and settings for the air cooling channels. [DOI: 10.1115/1.4055980]

Keywords: electrified propulsion, electric motor, interior permanent magnet (IPM) motor, air cooling, aviation fans, high altitude, low-pressure environment, air cooling channel size

1 Introduction

The Air Transport Action Group published a vision "Waypoint 2050X" [1], which stated the commercial aviation industry plans to decarbonize and achieve worldwide complete net-zero emissions by 2050. The International Air Transport Association including aircraft manufacturers, engine manufacturers, airports, and air traffic management, declared adoption of this goal [2,3] to support the United Nations Climate Change Conference (COP26). One of the innovations to decarbonize technology is electrification of aircraft propulsion systems. Felder at the National Aeronautics and Space Administration presented six promising types of aircraft electric propulsion systems [4].

- Type 1: All-electric, in which batteries drive electric motor-powered fans.
- Type 2: Parallel hybrid, in which battery-powered electric motors assist turbofans.
- Type 3: Turbo-electric, in which gas turbines generate electricity and their electricity drives electric motor-powered fans.
- Type 4: Series hybrid, in which gas turbines generate electricity, batteries provide electricity, and both electricity sources drive electric motor-powered fans.
- Type 5: Partial turbo-electric, in which turbofans generate electricity and their electricity drives additional electric motor-powered fans.
- Type 6: Series/partial hybrid, in which turbofans generate electricity, batteries provide electricity, and both sources drive additional electric motor-powered fans.

Currently, many companies are developing short-range aircraft with all-electric propulsion systems, such as those in Refs. [5–7], because all-electric systems are the simplest propulsion devices. The power density of cutting-edge batteries was 400 Wh/kg in 2021 [8], which is less than the 12,000 Wh/kg of kerosene. Thus, all-electric propulsion devices can be used only for short-range aircraft due to weight limitations for flight; in 2021, there are no aircraft with all-electric propulsion flying regional or longer ranges. Even by the 2030s, it would be difficult to realize

---

single-aisle aircraft with all-electric propulsion and approximately 150 passenger seats.

However, single-aisle aircraft with partial turbo-electric propulsion will be possible in the 2030s, so there are many concepts for developing single-aisle aircraft with partial turbo-electric propulsion by the 2030s. One of the promising single-aisle aircraft with partial turbo-electric propulsion is the STARC-ABL [9]. Figure 1 shows the targeted single-aisle tube- and wing-configuration with attached generators and with a ducted, electrically driven, boundary layer-ingesting tailcone fan. Boundary layer ingestion realizes a high propulsive efficiency η_{pro}. Here, an electric motor used to drive the tailcone fan must output approximately 2 MW. In addition, this electric motor must be a lightweight and high-power density ($=$ output/mass, W/kg) motor to enable flight. Furthermore, the electric motor must be air-cooled because there is no oil-lubricated gas turbine engine near the tail, unlike cases with attached generators. We have two choices in selecting the electric motor: superconductive motors and normal conductive motors. Although a superconductive motor is extremely lightweight and can operate at a gradually higher temperature than before [10], cryogenic cooling is required, and air cooling is not sufficient. Thus, superconductive motors look promising, but unfortunately, they are still a future technology at this time in the early 2020s. Among normal conductive motors, an interior permanent magnet (IPM) motor is presumed to be the best choice because of its simpler structure, higher efficiency, and higher power density.

Here, when the temperature of a permanent magnet exceeds its own maximum temperature limit, its magnetic flux density gradually decreases and does not recover. It is called "thermal demagnetization." Aircraft fly at a high altitude of 13,000 m (42,650 ft), where the ambient pressure decreases to 16 kPa (2.3 psi) in an intercontinental cruise, and aircraft can take off from an airport in a desert during summer at a high temperature of 50 °C (122 °F). Under any conditions, a reliable design method for thermal management of an air-cooled electric motor is essential to prevent permanent demagnetization.

Many researchers have studied thermal management of electric motors with experimental approaches [11], with numerical approaches [12,13], and with both [14]. These approaches are very important and effective, but they are overly time-consuming for the early design phase; instead, theoretical approaches are very convenient and provide results quickly with changing design parameters.

In early designs of electric motors, thermal analyses using a thermal circuit model were most common, such as in Ref. [15]. On the other hand, in early designs for heat exchangers, several differential equations were formulated for heat balancing with all fluid flows, this system of differential equations was mathematically integrated, and the results (i.e., temperature distributions, heat flow rates, pressure losses, etc.) were obtained as in Refs. [16–20]. Tao et al. also applied the latter approach to perform thermal management of entire electric automobiles, including an electric motor, but they used MATLAB/SIMULINK and AMESIM to solve this system of differential equations [21].
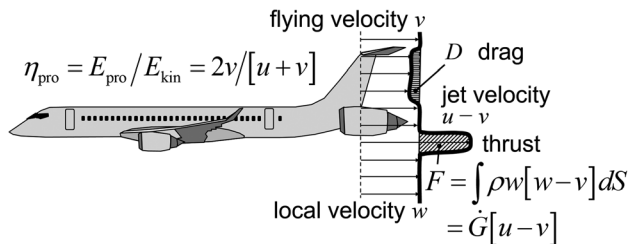
The authors and colleagues have advanced the latter approach using differential equations to analyze an air-cooled electric IPM motor driving an aviation fan and obtained transient solutions of the mathematical analytical equations instead of numerical solutions [22]; the mathematical analytical equations instantaneously derive the solution values without iterations, unlike numerical solutions. Then, the authors and colleagues obtained steady solutions with numerical time integration of the transient solutions. These solutions can be useful in allowing engineers to design air-cooled IPM motors early in design because steady solutions can be obtained quickly by using Microsoft Excel on a personal computer. Using this method, the authors discussed the capability and limitations of air cooling for the target IPM motor. From the results, the following predictions were made [22]: (1) internal recirculating air and external air should be separated inside and outside of the motor casing so electric parts in the casing also remain safe. (2) The internal air should move heat from the rotor to the outer heat exchanger, the heat exchanger should collect heat from the stator, and the external air should move all heat from the heat exchanger to the surroundings. (3) In the heat exchanger, the external air should flow between a stator and the internal air, and the flow direction of the external air should be opposite that of the internal air. (4) The internal air mass flowrate should be chosen to maintain turbulent internal flow through the heat exchanger. (5) There is the optimum flowrate of the internal air to minimize the rotor temperature. (6) The rotor temperature increases with decreasing internal air mass flowrate below the optimum value. (7) The rotor temperature increases with increasing internal air mass flowrate beyond the optimum value. (8) The rotor and stator temperatures are linearly proportional to the ambient temperature. (9) The rotor temperature increases with decreasing ambient pressure. (10) An increase in altitude causes a decrease in power consumption for both external air and internal air. (11) The most severe condition is the top-of-climb condition, and external and internal air mass flow rates should be chosen to keep the temperature of the permanent magnets below the maximum temperature limit of 100 °C and the temperature of the coils below the maximum temperature limit of 250 °C.

The above predictions were obtained for constant air-cooling channel sizes; however, the authors noticed that the sizes of air-cooling channel strongly affected air-cooling performance in the IPM motor. A designer has several choices for air-cooling channel sizes in the heat exchanger for internal and external air and choices for inner air-cooling channel sizes in the rotor. In this paper, the authors first briefly review the mathematical formulations and their solutions, then investigate the effect of channel size on air-cooling performance in the IPM motor, and finally explore the optimum configuration and settings for the air-cooling channels.

2 Targeted Air-Cooled Electric Motors Driving Aviation Fans

This section describes a targeted air-cooled IPM motor driving an aviation fan. Assumptions used to derive mathematical formulations and their solutions are defined.

2.1 Interior Permanent Magnet Motors Using Normal Conductors. The IPM motor is an alternating current synchronous electric motor. Figure 2 shows a schematic of the IPM motor. In general, a rotor is located inside a stator with a cylindrical shape. In the rotor, permanent magnets are placed inside a yoke made of a pile of magnetic steel sheets, from which the name "IPM" is derived. Permanent magnets do not require electricity. This method has many merits: there is no Joule heating loss, no electrical wiring, and no brush, and the system features a simple structure. The yoke concentrates its magnetic force on the surface of the rotor. Therefore, the rotor efficiency of the IPM motor is increased, and the rotor can be very compact. In addition,

$$\eta_{pro} = E_{pro}/E_{kin} = 2v/[u+v]$$

flying velocity v

D drag

jet velocity $u-v$

thrust

$$F = \int \rho w[w-v] dS$$

local velocity w

$$= \dot{G}[u-v]$$

Fig. 1 Partial turboelectric with boundary layer ingestion by air-cooled IPM motor-driven tailcone fan to achieve higher propulsive efficiency, η_{pro}

compared with surface permanent magnetic motors, the IPM motor can operate at a higher rotational rate because the permanent magnets are held tight by the yoke against a centrifugal force. Furthermore, the IPM motor rotor rotates synchronously with the frequency of a rotating magnetic field composed of electric coils under a wide range of loads. Thus, the rotation rate is highly controllable.

As a permanent magnet, a "neodymium magnet" made of $Nd_2Fe_{14}B$ is the best choice because it has the strongest magnetic flux of approximately 1.3 T, which is the value for a mass-produced neodymium magnet. The most advanced neodymium magnet with an EH or VH suffix can be used at a temperature of approximately 200 °C (392 °F), which is given as the catalog value [23]. However, this catalog value corresponds to the maximum allowable temperature when a neodymium magnet is positioned without a magnetic field, but the maximum allowable temperature must be lower to prevent demagnetization when a neodymium magnet is placed in a strong magnetic field such as a rotor in an IPM motor. Therefore, we set the maximum operating temperature of the neodymium magnet to 100 °C based on the experiences of our colleagues. In the rotor, heat is generated by hysteresis loss and eddy-current loss. The generated heat from the hysteresis loss and the eddy-current loss is relatively small compared with the Joule heating loss in the target condition, although these losses depend on operating conditions such as the rotational speed, power, voltage, current, and shape of each component.

In the stator, there are electromagnetic coils and a yoke, and heat is generated by Joule heating loss, hysteresis loss, and eddy-current loss. The Joule heating loss is dominant. To maintain the material health of the thermal insulators, we set the maximum operating temperature of the coils below a temperature of 250 °C (482 °F).

Consequently, more heat is generated in the stator than in the rotor of an IPM motor. Thus, the stator temperature is higher than the rotor temperature in general. In addition, the annular air layer between the rotor and stator is narrow due to electromagnetic performance, and direct heat transfer (DHT) via the annular air layer should count. Thermal barrier coatings on the outer surface of the rotor and the inner surface of the stator are effective in reducing direct heat transfer via the annular air layer.

For a targeted IPM motor, we presume the following factors:

Assumption 1. The output of the IPM motor is 2 MW. In a practical flight, the required output of the motor at the top-of-climb could be less than that at the takeoff. However, this design allows pilots to access the maximum output power at the top-of-climb; this constitutes safe redundancy.

Assumption 2. The rotational rate is 8000 rpm (i.e., 838 rad/s). In motor-driven fans, the rotation rate could be determined to suit the target thrust and flying velocity different from gas turbine-driven fans; thus, the rotation rate at the maximum output power was selected.

Assumption 3. The outer diameter of the rotor, d_{RL}, is 0.25 m, the outer diameter of the permanent magnets, d_{PML}, is 0.245 m, the inner diameter of the permanent magnets, d_{PMM}, is 0.20 m,
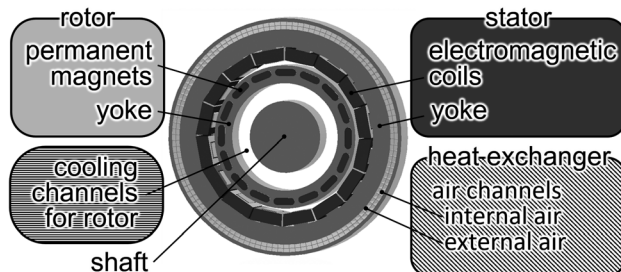
the inner diameter, d_{RM}, of the rotor's yoke is 0.15 m, and the shaft diameter, d_A, is 0.10 m. The yoke of the rotor is made of magnetic steel, and its thermal conductivity, λ_{steel}, is 50 W/(m·K). A thermal barrier coating (TBC) with a thickness, $\delta_{TBC,R}$, of 0.0005 m is placed on the outer surface of the rotor, a TBC with a thickness, $\delta_{TBC,S}$, of 0.0005 m is placed on the inner surfaces of the stator, and their thermal conductivities, $\lambda_{TBC,S}$ and $\lambda_{TBC,R}$, are 0.025 W/(m·K).

Assumption 4. An air layer with a thickness, δ_{Air}, of 0.001 m is between the TBCs. The inner diameter of the stator, d_{SM}, is $d_{RL} + 2(\delta_{TBC,R} + \delta_{Air} + \delta_{TBC,S})$, the outer diameter of the coils' section, d_{SCL}, is 0.30 m, and the outer diameter of the stator's yoke, d_{SL}, is 0.40 m. The length of both the stator and rotor, ℓ, is 0.50 m. The yoke of the stator is made of magnetic steel with λ_{steel} of 50 W/(m·K).

Assumption 5. A heat exchanger is placed outside of the stator, which has a two-story structure. External air flows through the channels on the floor closer to the stator, and internal air flows through the channels on the floor farther from the stator. Both channels of the heat exchanger, for internal and external air, have square shapes of $a \times b$ mm^2, and the number of channels is n. The channels are made of aluminum alloy, and the thermal conductivity of the heat exchanger, λ_{Al}, is 200 W/(m·K). The thickness, δ_f, of the floor of the heat exchanger attached on the outer surface of the stator is 0.005 m, and the thickness, δ_b, of the bulkhead between the external and internal air of the heat exchanger is 0.0005 m.

Assumption 6. The efficiency is 99% or higher, so the rotor produces a heat rate, Q_R, of 1 kW and the stator produces a heat rate, Q_S, of 15 kW. These values were derived by electromagnetic analyses corresponding to the maximum output and the worst case scenario. Other cases indicated lesser values of Q_R and Q_S even when the efficiency decreased because the output decreased more. With direct heat transfer, $Q_{S \to R}$, from the stator via the annular air layer to the rotor, cooling air flows should remove $Q_R + Q_{S \to R}$ from the rotor, and cooling air flows should remove $Q_S - Q_{S \to R}$ from the stator.

Assumption 7. The temperature of the rotor embedding permanent magnets never exceeds 100 °C, and the temperature of the stator does not exceed 250 °C.

2.2 Air-Cooling Configuration Schemes for Interior Permanent Magnet Motors.
The rotor is isolated from the motor casing, so internal air should cool the rotor. The outer shape of the rotor is fully cylindrical in a fixed stator. Many conventional motors undergo air cooling, in which air flow between the rotor and the stator cools the rotor. Such configurations that flow onto the outer surface of the rotor are Taylor–Couette or Taylor–Couette–Poiseuille flows [24]. However, there are several problems, which are described below.

Problem 1: The cylindrical channel between the rotor and stator is generally narrow to ensure electromagnetic performance; thus, the pressure loss is relatively large, and it is difficult to achieve a sufficiently large mass flowrate for the internal air flow through the cylindrical channel. A motor driving an aviation fan should have a small aspect ratio of its diameter/length to keep an airflow channel downstream of the fan; thus, the temperature of the internal air gradually increases in the axial direction until it reaches the rotor temperature, which occurs at the halfway point along the axial direction. At this point and beyond, the internal air does not cool the rotor because the air temperature is the same or higher than the rotor temperature.

Problem 2: In the targeted IPM motors, the stator generates heat, Q_S, larger than the heat, Q_R, generated by the rotor; thus, the temperature on the inner surface of the stator may be larger than the temperature on the outer surface of the rotor. In this case, the internal air no longer cools the rotor.

Instead, the inner surface of the rotor is useful in cooling, and the authors presume this air-cooling method for the rotor. The

Fig. 2   Schematic of an air-cooled IPM motor

authors determined which air-cooling configuration is best for an IPM motor in a previous paper [22]. Based on these results, the air-cooling configuration shown in Fig. 3 is best; first, internal recirculating air moves heat from the rotor to the heat exchanger attached outside of the stator, then the heat exchanger collects heat from the stator; next, the heat exchanger moves all heat to the external air, and finally, the external air moves all heat to the surroundings.

2.3 Air Physical Properties at an Arbitrary Temperature and Pressure.
Aircraft operate in all places across the Earth and must continue to operate even in severe conditions, such as in taking off from a desert in summer, which corresponds to an inlet temperature of $50\,°C$, or cruising at a high altitude of $13,000\,m$, where the air pressure is $16\,kPa$.

In this article, we presume that air is a perfect gas with a molar mass m_{mol} of $28.8 \times 10^{-3}\,kg/mol$ and a specific heat ratio of 1.4. In the pressure range $16–110\,kPa$ (corresponding to an altitude range of $0–13,000\,m$) at which almost all civil aircraft operate, the effects of pressure on viscosity and thermal conductivity are negligible, so viscosity μ_{air} (Pa·s) and thermal conductivity λ_{air} (W/(m K)) are estimated with Sutherland's equations [25]. Additionally, we presume
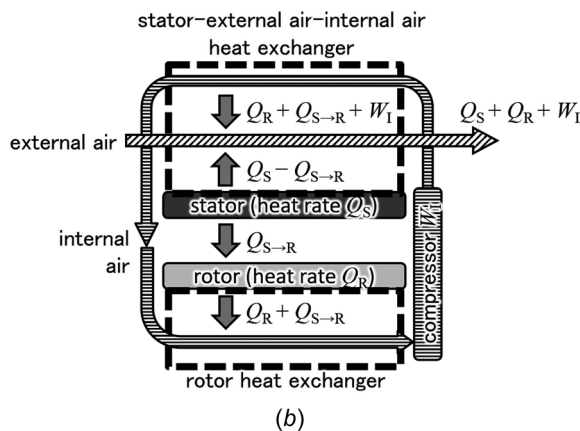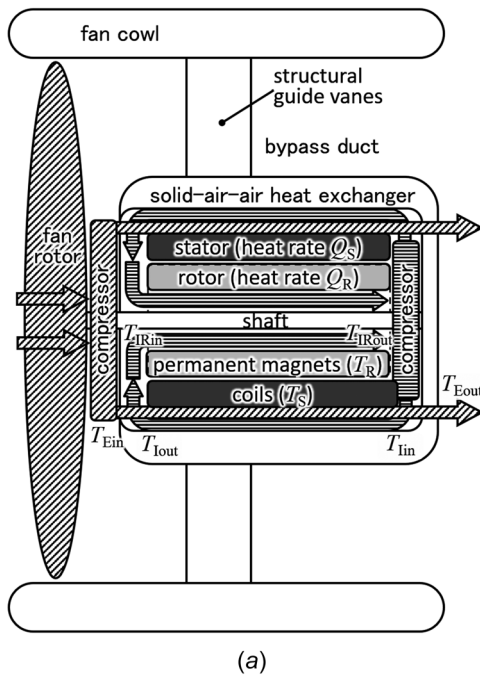

(a)

(b)

Fig. 3 Air-cooling schemes of IPM motors that drive aviation fans: (a) air-cooling scheme of the target IPM motor and (b) heat-transfer diagram of the target IPM motor

that air is incompressible over each air channel in the rotor or heat exchanger; namely, the physical properties of air are the same as values at the inlet of each air channel, and thus we presume:

Assumption 8. For internal air, the inlet pressure to the rotor is kept at ambient pressure. The outlet pressure from the rotor (corresponding to the inlet pressure to the internal compressor) is less than the ambient pressure due to pressure loss. The internal compressor compresses the internal air, and the outlet pressure from the internal compressor (corresponding to the inlet pressure to the heat exchanger) is the highest pressure in the system. The outlet pressure from the heat exchanger (corresponding to the inlet pressure to the rotor) returns to the ambient pressure.

Assumption 9. The fan and external compressor compress the external air, and the outlet pressure from the external compressor (corresponding to the inlet pressure to the heat exchanger) reaches the highest pressure. The outlet pressure from the heat exchanger decreases to ambient pressure due to pressure loss by the heat exchanger.

3 Mathematical Analytical Solutions for Temperatures of the Air-Cooled Interior Permanent Magnet Motor

This section derives the mathematical formulations for each heat-transfer process in the air-cooled IPM motor.

3.1 Direct Heat Transfer From the Stator Coils to the Rotor Permanent Magnets Via the Annular Air Layer.
Direct heat transfer, from the hot coils in the stator, via the inner surface of the stator, the thermal barrier coatings on the inner surface of the stator, the annular air layer, the thermal barrier coatings on the outer surface of the rotor, the outer surface of the rotor, and the electromagnetic steel to the cold permanent magnets in the rotor cannot be ignored. The heat transfer consists of conduction, convection, and radiation. In cases of the target temperature range, the effect of the radiation is less than the conduction and convection (see Appendix A1); here, the direct heat transfer by the conduction and convection is estimated.

First, the coefficient for heat transfer through the annular air layer between the stator coating and the rotor coating is estimated. Tachibana and Fukui performed extensive experiments on convective (including conductive) heat transfer between a stationary outer cylinder and a rotating coaxial inner cylinder [26]. They derived a correlation between Taylor number Ta and clearance Nusselt number Nu_{CL}

$$Nu_{CL} = 0.046[Ta^2 Pr]^{1/3} \qquad (1)$$

$$Ta^2 = \left\{ \frac{\rho_{air}[d_{RL} + 2\delta_{TBC,R}]\omega_R}{\mu_{air}} \frac{\delta_C}{2} \right\}^2 \frac{\delta_C}{d_{RL} + 2\delta_{TBC,R}} \qquad (2)$$

where ρ_{air} and μ_{air} are the density and viscosity of air, respectively, which are the average values of T_S and T_R. ω_R is the rotational rate of the rotor, and δ_C is the difference in diameter between coaxial cylinders of $d_{SM} - 2\delta_{TBC,S} - 2\delta_{TBC,R} - d_{RL}$. Nu_{CL} is defined as

$$Nu_{CL} = \frac{K_{air}}{\lambda_{air}} \frac{\delta_C}{2} \qquad (3)$$

where λ_{air} is the thermal conductivity at the average temperature of T_S and T_R. K_{air} is the coefficient for overall heat transfer via the annular air layer between two thermal barrier coatings. K_{air} is defined at $d_{RL} + 2\delta_{TBC,R}$ of the outer surface of the rotor coating.

Second, the coefficient for overall heat transfer $K_{S\rightarrow R}$ from the coils, via the thermal barrier coating, the annular air layer, the thermal barrier coating, and the yoke, to the permanent magnet is estimated. $K_{S\rightarrow R}$ is defined at d_{RL} of the outer surface of the rotor

$$K_{S \to R} = \cfrac{1}{\cfrac{d_{RL}}{2\lambda_{TBC,S}} \ln\left(\cfrac{d_{SM}}{d_{SM} - 2\delta_{TBC,S}}\right) + \cfrac{1}{K_{air}} \cfrac{d_{RL}}{d_{RL} + 2\delta_{TBC,R}} + \cfrac{d_{RL}}{2\lambda_{TBC,R}} \ln\left(\cfrac{d_{RL} + 2\delta_{TBC,R}}{d_{RL}}\right) + \cfrac{d_{RL}}{2\lambda_{steel}} \ln\left(\cfrac{d_{RL}}{d_{PML}}\right)} \tag{4}$$

Thus, the rate of heat flow $Q_{S \to R}$ between the coils and the permanent magnets is

$$Q_{S \to R} = \pi d_{RL} \ell_S K_{S \to R} [T_S - T_R] \tag{5}$$

3.2 Heat Transfer Between the Internal Air and the Rotor.

The rotor and shaft are mechanically connected, so they both rotate at the same rate ω (rad/s), as shown in Fig. 4. The rotor generates heat of Q_R (W), and the direct heat $Q_{S \to R}$ is added; the internal air recirculating in a motor case removes all heat via the inner surface of the rotor. This type of heat transfer was experimentally investigated by Seghir-Ouali et al. [27].

The peripheral length contacting the internal air with the rotor P_{IR} (m) normal to the axis is

$$P_{IR} = \pi d_{RM} \tag{6}$$

where d_{RM} (m) is the diameter of the inner surface of the rotor.

The axial velocity U_A through the rotor and tangential velocity U_R of the inner surface of the rotor are

$$U_A = \frac{\dot{m}_I}{\rho_{IR}} \frac{4}{\pi [d_{RM}^2 - d_A^2]}, \quad U_R = \frac{\omega d_{RM}}{2} = \pi \frac{X}{60} d_{RM} \tag{7}$$

where ω (rad/s) and X (rpm) are rotational rates of the rotor.

The axial Reynolds number Re_A and the rotational Reynolds number Re_R of the internal air through the rotor are

$$Re_A = \frac{\rho_{IR} U_A d_{RM}}{\mu_{IR}} = \frac{4\dot{m}_I}{\mu_{IR}} \frac{d_{RM}}{\pi [d_{RM}^2 - d_A^2]},$$
$$Re_R = \frac{\rho_{IR} U_R d_{RM}}{\mu_{IR}} = \frac{\rho_{IR} \omega d_{RM}^2}{2\mu_{IR}} = \frac{\pi \rho_{IR} d_{RM}^2 X}{60\mu_{IR}} \tag{8}$$

In cases of flows dominated by rotating flow compared with axial flow ($2.77 \times 10^5 \leq Re_R$), the experimental correlation between Nusselt and rotational Reynolds numbers proposed in Ref. [27] is

$$Nu_{P,R} = 2.85 \times 10^{-4} Re_R^{1.19} \tag{9}$$

In cases of flows affected by both axial flow and rotating flow ($1.6 \times 10^3 < Re_R < 2.77 \times 10^5$ and $0 < Re_R < 3 \times 10^4$), another experimental correlation was proposed in Ref. [27]

$$Nu_{P,R} = 1.963 \times 10^{-2} Re_A^{0.9285} + 8.51 \times 10^{-6} Re_R^{1.4513} \tag{10}$$

The heat transfer coefficient h_R is

$$h_R = Nu_{P,R} \frac{\lambda_{IR}}{d_R} \tag{11}$$

where λ_{IR} (W/(m K)) is the thermal conductivity of the internal air. K_R is the coefficient for overall heat transfer via the yoke and heat resistance on the inner surface of the rotor because the permanent magnets are placed inside the yoke. K_R is defined at d_{RM} of the inner surface of the rotor

$$K_R = \frac{1}{\frac{1}{h_R} + \frac{d_{RM}}{2\lambda_{steel}} \ln\left(\frac{d_{PMM}}{d_{RM}}\right)} \tag{12}$$

Figure 5 shows the temperature distribution in the axial direction through the rotor. The rotor is composed of magnetic steel sheets; thus, the thermal conductivity in the axial direction is much greater than that in air, and the temperature of the rotor can be presumed to be constant in the axial direction at $T_{R,t}$ (K). On the other hand, the temperature T_{IRx} (K) of the internal air is increased by heat received from the inner surface of the rotor. At position x (m) in the axial direction from the inlet of the rotor, the local heat flux q_{IRx} (W/m^2) for an infinitesimal region in the axial direction with a length of dx (m) is

$$q_{IRx} = \dot{m}_I C_P dT_{IRx} = K_R [T_{R,t} - T_{IRx}] P_{IR} dx \tag{13}$$

where C_P (J/(kg K)) is the specific heat of the internal air. Then

$$\frac{dT_{IRx}}{T_{IRx} - T_{R,t}} = \frac{-P_{IR} K_R}{\dot{m}_I C_P} dx \tag{14}$$

Integrating both sides gives

$$T_{IRx} - T_{R,t} = c_0 \exp\left(\frac{-P_{IR} K_R}{\dot{m}_I C_P} x\right) \tag{15}$$

where c_0 is an integration constant. By applying the boundary condition $T_{IRx} = T_{IRin}$ at $x = 0$

$$T_{IRx} = T_{R,t} + [T_{IRin} - T_{R,t}] \exp\left(\frac{-P_{IR} K_R}{\dot{m}_I C_P} x\right) \tag{16}$$

Then, another boundary condition $T_{IRx} = T_{IRout}$ is applied at $x = \ell_R$; finally, the outlet temperature T_{IRout} of the internal air is solved analytically

$$T_{IRout} = T_{R,t} + [T_{IRin} - T_{R,t}] \exp\left(\frac{-P_{IR} K_R}{\dot{m}_I C_P} \ell_R\right) \tag{17}$$

Next, the energy balance of the internal air through the rotor is considered

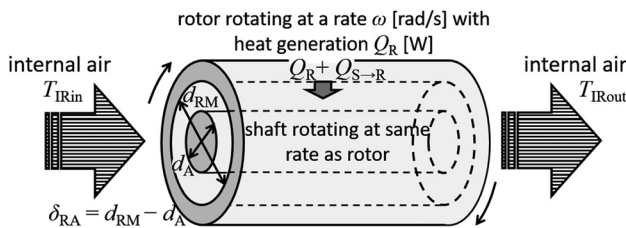$$\dot{m}_I C_P [T_{IRout} - T_{IRin}] = Q_{I \leftarrow R} \tag{18}$$

Fig. 4 Convective heat transfer between a rotating cylinder inner surface of the rotor and the internal air flowing axially inside the rotor
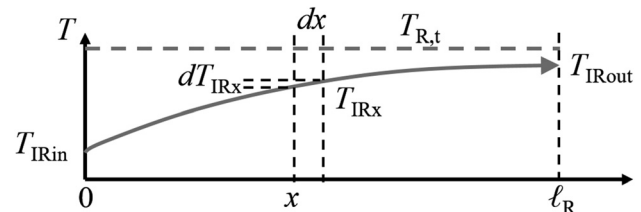

Fig. 5 Schematic of temperature distributions in the axial direction through the rotor

In addition, the energy balance of the rotor is considered

$$m_R C_{P,R} dT_{R,t} = [Q_R + Q_{S \to R} - Q_{I \gets R}] dt \quad (19)$$

where m_R (kg) is the mass of the rotor, $C_{P,R}$ (J/(kg·K)) is the specific heat of the rotor, and $T_{R,t}$ (K) is the temperature of the permanent magnets at time t (s). $T_{R,t}$ can be calculated over time; thus

Case 1: In cases of $Q_R + Q_{S \to R} > Q_{I \gets R}$, $T_{R,t}$ increases with time.

Case 2: In cases of $Q_R + Q_{S \to R} < Q_{I \gets R}$, $T_{R,t}$ decreases with time.

Case 3: In cases of $Q_R + Q_{S \to R} = Q_{I \gets R}$, $T_{R,t}$ is steady.

3.3 Heat Transfer Among the Stator, External Air, and Internal Air in the Heat Exchanger Attached Outside of the Stator.

Figure 6 shows a schematic for the configuration with a stator-external air-internal air heat exchanger. This heat exchanger is directly attached on the outer surface of the stator yoke. This heat exchanger consists of two-story structures: channels for the external air are located on the floor closer to the stator, and channels for the internal air are located further away on the floor. The stator generates heat of Q_S (W), and the direct heat of $Q_{S \to R}$ is subtracted. Solid structures of the stator yoke and the heat exchanger directly conduct heat generated by the stator to the external air from the bottom side. At the same time, the bulkhead of the heat exchanger passes heat from the internal air to the external air from the top side.

The axial velocities V_I and V_E of internal and external air passing through the heat exchanger are

$$V_I = \dot{m}_I \frac{1}{\rho_I} \frac{1}{n_I a_I b_I}, \quad V_E = \dot{m}_E \frac{1}{\rho_E} \frac{1}{n_E a_E b_E} \quad (20)$$

where $\dot{m}_I$ and $\dot{m}_E$ (kg/s) are mass flow rates, ρ_I and ρ_E (m^3/kg) are densities, n_I and n_E (m) are the numbers of channels, a_I and a_E are the heights, and b_I and b_E (m) are widths of the internal and external air channel, respectively.

Hydraulic diameters d_I and d_E (m) are

$$d_I = \frac{4S_I}{P_I} = \frac{4a_I b_I}{2a_I + 2b_I}, \quad d_E = \frac{4S_E}{P_E} = \frac{4a_E b_E}{2a_E + 2b_E} \quad (21)$$

where S_I and S_E (m^2) are the cross section and P_I and P_E (m) are the peripheral lengths of the internal and external air channel, respectively. Pipe Reynolds numbers $Re_{P,I}$ and $Re_{P,E}$ of the internal and external air through each channel in the heat exchanger are
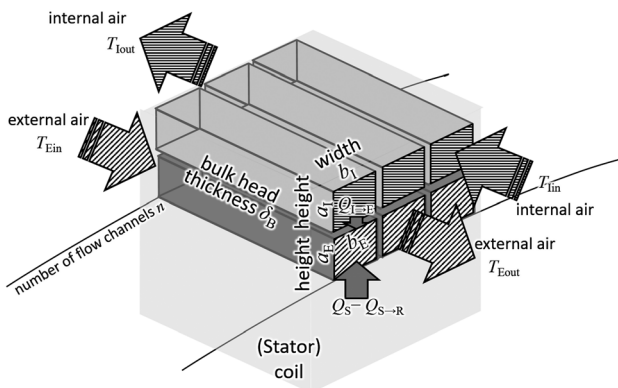

Fig. 6 Configurations of the stator-external air-internal air heat exchanger outside of the stator

$$Re_{P,I} = \frac{\rho_I V_I d_I}{\mu_I} = \frac{\rho_I}{\mu_I} \dot{m}_I \frac{1}{\rho_I} \frac{1}{n_I a_I b_I} \frac{4a_I b_I}{2a_I + 2b_I} = \frac{2\dot{m}_I}{\mu_I n_I \{a_I + b_I\}},$$

$$Re_{P,E} = \frac{\rho_E V_E d_E}{\mu_E} = \frac{2\dot{m}_E}{\mu_E n_E \{a_E + b_E\}} \quad (22)$$

Prandtl numbers Pr_I and Pr_E of the internal and external air passing through each air channel in the heat exchanger are

$$Pr_I = \frac{C_P \mu_I}{\lambda_I}, \quad Pr_E = \frac{C_P \mu_E}{\lambda_E} \quad (23)$$

The pipe Nusselt number $Nu_{P,I}$ of the internal air with fully developed temperature fields in laminar flow $(Re_{P,I} < 3000)$ or turbulent flow $(3000 \le Re_{P,I} < 10^7)$ in a pipe with a constant wall temperature is

$$Nu_{P,I} = 3.66 \quad (Re_{P,I} < 3000) \quad (24)$$

$$Nu_{P,I} = 0.023 Re_{P,I}^{0.8} Pr_I^{1/3} \quad (3000 \le Re_{P,I} < 10^7) \quad (25)$$

The pipe Nusselt number $Nu_{P,E}$ of the external air is

$$Nu_{P,E} = 3.66 \quad (Re_{P,E} < 3000) \quad (26)$$

$$Nu_{P,E} = 0.023 Re_{P,E}^{0.8} Pr_E^{1/3} \quad (3000 \le Re_{P,E} < 10^7) \quad (27)$$

Heat transfer coefficients h_I and h_E are

$$h_I = Nu_{P,I} \frac{\lambda_I}{d_I}, \quad h_E = Nu_{P,E} \frac{\lambda_E}{d_E} \quad (28)$$

where λ_I and λ_E (W/(m K)) are the thermal conductivities of the internal and external air, respectively. The heat transfer coefficient between the stator and the external air is h_E, and the overall heat transfer coefficient between the external air and the coil via the yoke is K_S (W/(m^2 K)). Here, K_S is defined at $d_{SL} + 2\delta_F$ for the floor closer to the stator of the heat exchanger

$$K_S = \frac{1}{\frac{1}{h_E} + \frac{d_{SL} + 2\delta_F}{2\lambda_{Al}} \ln\left(\frac{d_{SL} + 2\delta_F}{d_{SL}}\right) + \frac{d_{SL} + 2\delta_F}{2\lambda_{steel}} \ln\left(\frac{d_{SL}}{d_{SCL}}\right)} \quad (29)$$

The coefficient for overall heat transfer between the internal air and the external air via the bulkhead, K_B (W/(m^2 K)), is

$$K_B = \frac{1}{\frac{1}{h_I} + \frac{\delta_B}{\lambda_{Al}} + \frac{1}{h_E}} \quad (30)$$

where δ_B (m) is the thickness and λ_{Al} (W/(m K)) is the thermal conductivity of the bulkhead between the internal and external air.

Figure 7 shows a schematic for temperature distributions in the axial direction through this stator-external air-internal air heat
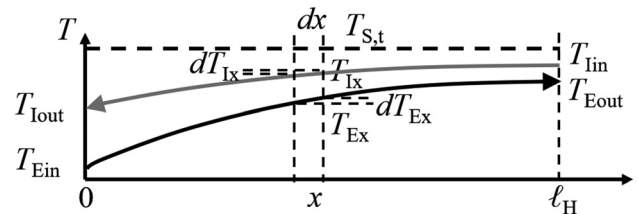

Fig. 7 Schematic of temperature distributions in the axial direction through the "stator-external air-internal air" heat exchanger

exchanger. At position x (m) in the axial direction from the left end of the heat exchanger, for an infinitesimal region in the axial direction with a length of dx (m), local heat flux $dq_{S\to Ex}$ (W/m) is exchanged between the stator and the external air, and local heat flux $dq_{I\to Ex}$ (W/m) is exchanged between the internal air and the external air. The coils are made of copper; thus, the thermal conductivity in the axial direction is much greater than that in air, and the temperature of the heat exchanger can be presumed to be constant in the axial direction at $T_{S,t}$ (K). The internal air flows in the opposite direction against the external air flow because this configuration increases the heat exchange efficiency. Namely, the internal air flows from the right end to the left end in Fig. 7. The temperature T_{Ix} (K) of the internal air decreases as heat $dq_{I\to Ex}$ is released to the external air via the bulkhead. On the other hand, the external air receives $dq_{S\to Ex}$ from the stator and $dq_{I\to Ex}$ from the internal air via the bulkhead at the same time. Thus, the temperature T_{Ex} (K) of the external air increases. Based on these characteristics, the energy balances of the internal and external air are

$$\dot{m}_E C_P dT_{Ex} = nbK_B[T_{Ix} - T_{Ex}]dx + nbK_S[T_{S,t} - T_{Ex}]dx \quad (31)$$

$$\dot{m}_I C_P dT_{Ix} = nbK_B[T_{Ix} - T_{Ex}]dx \quad (32)$$

These equations are simultaneously solved for T_{Ex} and T_{Ix}; thus, we apply boundary conditions of $T_{I0} = T_{Iout}$ and $T_{E0} = T_{Ein}$ at $x = 0$ and $T_{I\ell R} = T_{Iin}$ and $T_{E\ell R} = T_{Eout}$ at $x = \ell_R$ (see Ref. [22] for details). Then, the analytical solutions are obtained from [22]

$$T_{Eout} = \frac{-\zeta\sigma_2}{2K_B N\beta} + \tilde{C}_E \frac{\zeta\exp(\beta\ell_S)}{2K_B N} + \frac{-\xi\theta_2}{2K_B N\gamma} + \tilde{C}_I \frac{\xi\exp(\gamma\ell_S)}{2K_B N} \quad (33)$$

$$T_{Iout} = \frac{-\sigma_2}{\beta} + \tilde{C}_E + \frac{-\theta_2}{\gamma} + \tilde{C}_I \quad (34)$$

where the combined variables are

$$\tilde{C}_E = \frac{\sigma_2}{\beta} + \frac{\xi\theta_2}{\zeta\gamma} + \frac{-\tilde{C}_I\xi}{\zeta} + \frac{2K_B N}{\zeta}T_{Ein}, \quad \tilde{C}_I = \frac{T_{Iin} + \frac{\sigma_2}{\beta}\{1 - \exp(\beta\ell_S)\} + \frac{\theta_2}{\gamma}\left\{1 - \frac{\xi}{\zeta}\exp(\beta\ell_S)\right\} + \frac{-2K_B N}{\zeta}\exp(\beta\ell_S)T_{Ein}}{\exp(\gamma\ell_S) + \frac{-\xi}{\zeta}\exp(\beta\ell_S)},$$

$$N = \frac{nbK_B}{\dot{m}_E C_P}, \quad \varepsilon = \frac{\dot{m}_I C_P}{\dot{m}_E C_P}, \quad \phi = -\varepsilon K_S - \varepsilon K_B + K_B, \quad \psi = \varepsilon K_S + \varepsilon K_B + K_B, \quad \alpha = N\sqrt{\phi^2 + 4\varepsilon K_S K_B},$$

$$\xi = N\psi - \alpha, \quad \beta = \frac{N\phi - \alpha}{2\varepsilon K_B}, \quad \gamma = \frac{N\phi + \alpha}{2\varepsilon K_B}, \quad \zeta = N\psi + \alpha, \quad \sigma_2 = \frac{N^2 K_S}{\alpha}T_{S,t}, \quad \theta_2 = \frac{-N^2 K_S}{\alpha}T_{S,t} \quad (35)$$

Here, energy balance among the internal air, the external air, and the stator are considered. The exchange heat $Q_{I\to E}$ transferred from internal to external air is equal and opposite to the heat Q_I received by the internal air; thus

$$\dot{m}_I C_P[T_{Iout} - T_{Iin}] = Q_I = -Q_{I\to E} \quad (36)$$

The sum of the exchange heat $Q_{I\to E}$ and exchange heat $Q_{S\to E}$ from the stator to external air equals the heat Q_E received by the external air; thus

$$\dot{m}_E C_P[T_{Eout} - T_{Ein}] = Q_E = Q_{I\to E} + Q_{S\to E} \quad (37)$$

The sum of the exchanged heat $Q_{S\to E}$ and heat generation rate Q_S in the stator changes the stator temperature $T_{S,t}$; thus

$$m_S C_{P,S}\frac{dT_{S,t}}{dt} = Q_S - Q_{S\to R} - Q_{S\to E} = Q_S - Q_{S\to R} - Q_I - Q_E \quad (38)$$

where m_S (kg) is the mass of the stator, $C_{P,S}$ (J/(kg K)) is the specific heat of the stator, and $T_{S,t}$ (K) is the temperature of the coils at time t (s). Therefore, $T_{S,t}$ can be calculated over time, so

Case 1: In cases of $Q_S - Q_{S\to R} > Q_I + Q_E$, $T_{S,t}$ increases with time.
Case 2: In cases of $Q_S - Q_{S\to R} < Q_I + Q_E$, $T_{S,t}$ decreases with time.
Case 3: In cases of $Q_S - Q_{S\to R} = Q_I + Q_E$, $T_{S,t}$ is steady.

4 Pressure Loss and Power Consumption of Cooling Air in the Air-Cooled Interior Permanent Magnet Motor

This section estimates the pressure difference for each air-cooling channel contained in the targeted air-cooled IPM motor.

4.1 Pressure Loss and Power Consumption of Internal Air Passing Through the Rotor.
As mentioned in Sec. 3.2 and as shown in Fig. 4, the rotor and shaft are mechanically connected, and they rotate at the same rate. Here, pressure loss through the rotor is considered. Yamada and Watanabe performed extensive experiments with this kind of flow, and they evaluated the pressure loss coefficient f_{IR} with coaxial Reynolds number Re_C and rotational Reynolds number Re_R [28]. The definition of Re_R is the same as in Eq. (8), but coaxial Reynolds number $Re_{d,C}$ is newly defined. Here, the inner diameter of the rotor is d_{RM}, the outer diameter of the shaft is d_A, and the difference between d_{RM} and d_A is δ_C. By considering a hydraulic diameter d_C (m) of the channel between the coaxial cylinders

$$d_A = d_{RM} - \delta_C$$
$$S = \frac{\pi d_{RM}^2 - \pi d_A^2}{4} = \frac{\pi d_{RM}^2 - \pi\{d_{RM} - \delta_C\}^2}{4} = \frac{\pi\delta_C\{2d_{RM} - \delta_C\}}{4}$$
$$P = \pi d_{RM} + \pi d_A = \pi d_{RM} + \pi\{d_{RM} - \delta_C\} = \pi\{2d_{RM} - \delta_C\}$$
$$d_C = \frac{4S}{P} = \delta_C = d_{RM} - d_A \quad (39)$$

where S (m^2) is the cross section of the channel and P (m) is the peripheral length of the channel. Namely, the hydraulic diameter d_C of the channel between the coaxial cylinders equals the difference δ_C between d_{RM} and d_A. Thus, the coaxial Reynolds number Re_C for the internal air passing through the rotor is

$$Re_C = \frac{\rho_I V_I d_C}{\mu_I} = \frac{4\dot{m}_I\{d_{RM} - d_A\}}{\mu_I\pi\{d_{RM}^2 - d_A^2\}} = \frac{4\dot{m}_I}{\mu_I\pi\{d_{RM} + d_A\}} \quad (40)$$

Yamada and Watanabe mentioned that f_{IR} is almost the same as f_{IR} for no rotation even in laminar and turbulent flows in cases

where $\mathrm{Re_C}$ is not very small and both cylinders rotate at the same rate [28]. Therefore, the pressure loss coefficient f_IR is

$$f_\mathrm{IR} = \frac{96}{\mathrm{Re_C}} \tag{41}$$

for laminar flows, and

$$f_\mathrm{IR} = 0.316\mathrm{Re_C^{-1/4}} \tag{42}$$

for turbulent flows.

Yamada and Watanabe also mentioned that a transient $\mathrm{Re_C}$ changes with $\mathrm{Re_R}$ as laminar flow changes to turbulent flow [28]; however, we presume laminar flows in cases of $0 < \mathrm{Re_C} < 2000$ and turbulent flows in cases of $2000 \leq \mathrm{Re_C}$ based on experimental results reported by Yamada and Watanabe [28]. Here, the total pressure loss Δp_lossIR (Pa) is

$$\Delta p_\mathrm{lossIR} = f_\mathrm{IR} \frac{\rho_\mathrm{IR} V_\mathrm{IR}^2}{2} \frac{\ell_\mathrm{R}}{\delta_\mathrm{C}} \tag{43}$$

4.2 Pressure Loss and Power Consumption of the Internal and External Air Passing Through the Heat Exchanger Attached Outside of the Stator. As shown in Fig. 6, the channels for internal air and external air are rectangular with a height of a and width of b; thus, hydraulic diameters d_I and d_E and pipe Reynolds numbers $\mathrm{Re_{P,I}}$ and $\mathrm{Re_{P,E}}$ were defined in Eq. (22). The total pressure loss is estimated with the Hargen–Poiseuille and Blasius equations in association with the Darcy–Weisbach equation.

Pressure loss coefficients f_I and f_E are

$$f_\mathrm{I} = \frac{64}{\mathrm{Re_{P,I}}}, \quad f_\mathrm{E} = \frac{64}{\mathrm{Re_{P,E}}} \tag{44}$$

for laminar flows ($\mathrm{Re_{P,I}} < 3000$ or $\mathrm{Re_{P,E}} < 3000$), and

$$f_\mathrm{I} = 0.316\mathrm{Re_{P,I}^{-1/4}}, \quad f_\mathrm{E} = 0.316\mathrm{Re_{P,E}^{-1/4}} \tag{45}$$

for turbulent flows ($3000 \leq \mathrm{Re_{P,I}}$ or $3000 \leq \mathrm{Re_{P,E}}$).

Total pressure losses Δp_lossIH and Δp_lossEH (Pa) are

$$\Delta p_\mathrm{lossIH} = f_\mathrm{I} \frac{\rho_\mathrm{I} V_\mathrm{I}^2}{2} \frac{\ell_\mathrm{H}}{d_\mathrm{I}}, \quad \Delta p_\mathrm{lossEH} = f_\mathrm{E} \frac{\rho_\mathrm{E} V_\mathrm{E}^2}{2} \frac{\ell_\mathrm{H}}{d_\mathrm{E}} \tag{46}$$

4.3 Effect on the Energy Balance of Power Consumption by Compressors for Internal and External Air. As shown in Fig. 3, a fan and external compressor force the external air through the heat exchanger with power consumption W_E

$$W_\mathrm{E} = \frac{\dot{m}_\mathrm{E}}{\rho_\mathrm{Ein}\eta_\mathrm{compE}} \Delta p_\mathrm{lossEH} \tag{47}$$

where ρ_Ein is the density at the fan inlet and η_compE is the adiabatic efficiency of the fan and external compressor. Power W_E increases the temperature T_Ein at the inlet of the heat exchanger

$$T_\mathrm{Ein} = T_\mathrm{amb} + \frac{T_\mathrm{amb}}{\eta_\mathrm{E}} \left[\left\{ \frac{p_\mathrm{amb} + \Delta p_\mathrm{lossEH}}{p_\mathrm{amb}} \right\}^{\frac{\gamma-1}{\gamma}} - 1 \right] \tag{48}$$

As shown in Fig. 3, another internal compressor recirculates the internal air. The power W_I consumed to force the internal air through the rotor and the heat exchanger is

$$W_\mathrm{I} = \frac{\dot{m}_\mathrm{I}}{\rho_\mathrm{IRout}\eta_\mathrm{compI}} [\Delta p_\mathrm{lossIH} + \Delta p_\mathrm{lossIR}] \tag{49}$$

where ρ_IRout is the density at the inlet of the internal compressor and η_compI is the adiabatic efficiency of the internal compressor.

Power W_I increases the temperature T_Iin at the inlet of the heat exchanger and also increases the heat $Q_\mathrm{I \to E}$ exchanged from the internal to external air because this power W_I is ultimately converted into heat; thus

$$Q_\mathrm{I \to E} = Q_\mathrm{R} + Q_\mathrm{S \to R} + W_\mathrm{I} \tag{50}$$

$$T_\mathrm{Iin} = T_\mathrm{IRin} + \frac{Q_\mathrm{R} + Q_\mathrm{S \to R} + W_\mathrm{I}}{m_\mathrm{I} C_\mathrm{P,I}} \tag{51}$$

Equation (51) indicates that the power consumption W_I affects the rotor temperature T_R.

5 Effect of Direct Heat Transfer and Heat Resistance on Air-Cooling Performance

This section evaluates the current model used to consider direct heat transfer from the coils to permanent magnets and heat resistance in the stator and rotor compared with those of the conventional model described in Ref. [22]. Validation of the current model is described in Appendix A2.

5.1 Difference Between the Current Model and the Authors' Conventional Model. To obtain mathematical analytical solutions that maintain the maximum temperature limits for permanent magnets in the rotor and coils in the stator, the authors and colleagues introduced a mathematical model that describes heat transfer inside the targeted air-cooled IPM motor [22]. The solutions indicated many characteristics and provided considerable knowledge regarding the targeted IPM motor under severe operational conditions, such as top-of-climb.

However, as shown in Table 1, the temperature in the entire rotor at the permanent magnets and the inner heat-transfer surface were assumed to be constant in the conventional model. The temperature over the entire stator at the coils and the outer heat-transfer surface were also assumed to be constant. In practical situations, temperatures at the permanent magnets and coils must be higher than that in the isothermal stator and rotor because both the rotor and stator have internal heat resistance. In addition, in the model in Ref. [22], the rate of direct heat transfer from the stator coils via the annular air layer to the rotor permanent magnets was implied for the constant heat generated from the stator and rotor. In practical situations, the rate of direct heat transfer must be altered based on the temperature difference between the coils and permanent magnets.

Instead, in this paper, the authors introduce Eqs. (12) and (29) to describe the internal heat resistance in the rotor and stator and Eqs. (1)–(5) to describe the variable rate for direct heat transfer based on the temperature difference between the coils and permanent magnets.

5.2 Effect of the Air Mass Flow Rate on Temperatures of the Permanent Magnet and Coil. Figure 8 compares the results estimated with the current model (solid curves) and with the conventional model (dashed curves). The left figures show the temperature changes in permanent magnets T_R (in blue) and coils T_S (in red) with changes in the mass flowrate of a focused air flow in the horizontal axis, and the right figure shows the power consumption needed to drive the external air W_E (in green) and the internal air W_I (in orange) corresponding to T_R in the vertical axis. Refer to Ref. [22], where the detailed tendencies were explained. Differences between the results of the current model and the conventional model are considered in Sec. 5.

Figure 8(a) shows the results for cases with a constant external air mass flowrate of $1.4\,\mathrm{kg/s}$. The coil temperature T_S (red solid curve) estimated by the current model is higher than the T_S (red dashed curve) estimated by the conventional model because of heat resistance from the coils to the external air via the magnetic steel and the heat exchanger. In the region where $\dot{m}_\mathrm{I} \geq 0.07\,\mathrm{kg/s}$

Table 1 Characteristics of models used to estimate air-cooling performance for the targeted IPM motor

Physics	Current model	Conventional model in Ref. [22]
Heat resistance of electromagnetic steel between the rotor inner surface and the permanent magnets when calculating the heat exchange rate between the permanent magnets and the internal air	Considered	Not considered
Heat resistance of electromagnetic steel and aluminum between the coils and the air channel surfaces of the heat exchanger when calculating the heat exchange rate between the coils and the external air	Considered	Not considered
DHT between the coils and the permanent magnets in the rotor	Considered	Not considered
Heat resistance of the thermal barrier coating on the stator inner surface when calculating DHT	Considered	Not considered
Heat resistance of the thermal barrier coating on the rotor outer surface when calculating DHT	Considered	Not considered
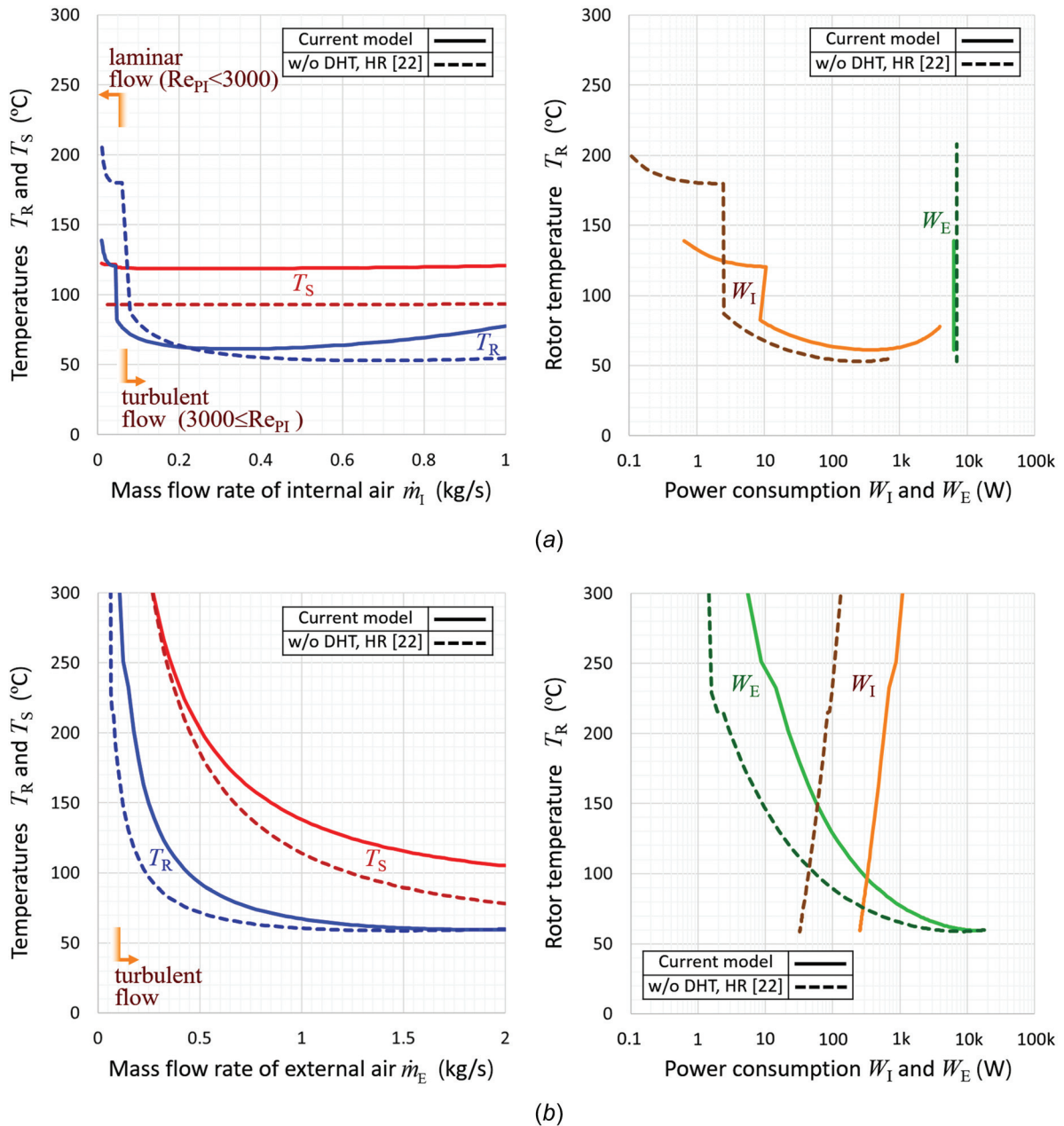
Fig. 8   Permanent magnets and coil temperature as well as power consumption with changing air mass flow rates estimated with the conventional model and the current model (d_R = 150 mm, d_A = 100 mm, δ_{TBC} = 0.5 mm, δ_{AIR} = 1 mm, $a_E = b_E$ = 10 mm, $a_I = b_I$ = 10 mm): (*a*) cases with a constant external air mass flow rate $\dot{m}_E$ of 1.4 kg/s and (*b*) cases with a constant internal air mass flow rate $\dot{m}_I$ of 0.28 kg/s

(solid curve) or $\dot{m}_I \geq 0.045$ kg/s (dashed curve), the internal air flow is turbulent in the heat exchanger, and heat is exchanged well. Thus, as shown in Fig. 3, the inlet temperature T_{IRin} of the rotor sufficiently decreased, and the permanent magnets were well cooled, so T_R was always lower than T_S. Instead, in the region where $\dot{m}_I < 0.07$ kg/s (solid curve) or $\dot{m}_I < 0.045$ kg/s (dashed curve), the internal air flow is laminar in the heat exchanger, and heat is not exchanged sufficiently. Thus, as shown in Fig. 3, the inlet temperature T_{IRin} of the rotor is relatively high, and the permanent magnets are not sufficiently cooled, so T_R has a gap within this region of $\dot{m}_I$.

Direct heat transfer $Q_{S \rightarrow R}$ flows from the hotter part to the colder part. In the turbulent region of $\dot{m}_I$, the coil temperature T_S is higher than the permanent magnet temperature T_R; thus, $Q_{S \rightarrow R}$ is positive, and the temperature difference of T_S (red solid curve) $- T_R$ (blue solid curve) estimated by the current model is greater than that of T_S (red dashed curve) $- T_R$ (blue dashed curve) estimated by the conventional model. On the other hand, in the laminar region of $\dot{m}_I$, the coil temperature T_S is lower than the permanent magnet temperature T_R; thus, $Q_{S \rightarrow R}$ is negative, and the temperature difference of T_R (blue solid curve) $- T_S$ (red solid curve) estimated by the current model is smaller than that of T_R (blue dashed curve) $- T_S$ (red dashed curve) estimated by the conventional model.

An increase in $\dot{m}_I$ causes a decrease in the permanent magnet temperature T_R in a smaller $\dot{m}_I$ region because the pipe Reynolds number $Re_{P,I}$ and Nusselt number $Nu_{P,I}$ increase and the internal air is cooled better through the heat exchanger. Then, in a larger $\dot{m}_I$ region, an increase in $\dot{m}_I$ causes a rebound in the permanent magnet temperature T_R because the pressure loss used to recirculate the internal flow increases and the power consumption W_I increases. W_I is finally converted into heat in the internal air, and this heat should be transferred from the internal air to the external air. Therefore, the permanent magnet temperature T_R gradually increases.

Figure 8(b) shows the results for cases with a constant internal air mass flowrate of 0.28 kg/s. Under this condition, the flow of internal air through the heat exchanger is always turbulent so the coil temperature T_S is higher than the permanent magnet temperature T_R; thus, $Q_{S \rightarrow R}$ is positive, and T_S (red solid curve) estimated by the current model is higher than T_S (red dashed curve) estimated by the conventional model.

Although the internal air mass flowrate $\dot{m}_I$ is constant, the power W_I (orange curves) consumed by the internal air decreases with increasing $\dot{m}_E$ (corresponding to decreasing T_R). This is because an increase in $\dot{m}_E$ causes a decrease in the temperature of the entire system; thus, the internal air is cooled better, its density increases, its velocity decreases and W_I decreases.

5.3 Effect of Ambient Temperature on Air-Cooling Performance. Figure 9 shows the effect of the ambient temperature T_{amb} on air-cooling performance, i.e., the results for T_R (light gray curves) and T_S (dark gray curves) and the power consumed by internal air flow W_I (light gray curves) and external air flow W_E (dark gray curves) with T_{amb} in the case of constant volume flow rates $\dot{V}_E$ of 1.4 m³/s and $\dot{V}_I$ of 0.32 m³/s, which correspond to $\dot{m}_E = 1.7$ kg/s and $\dot{m}_I = 0.34$ kg/s at the ambient temperature T_{amb} of 15 °C and the ambient pressure p_{amb} of 101.3 kPa. The reason why volume flow rates $\dot{V}_E$ and $\dot{V}_I$ are fixed is that a compressor operating at a constant rotational rate generally discharges a constant volume flowrate when the inlet temperature and pressure change. For practical flight, the temperature at takeoff has a wide range, from -40 °C (at an airport in a polar region in winter) to 50 °C (at an airport in a desert region in summer), so we estimate T_R and T_S in this temperature range. As expected, a higher T_{amb} results in higher T_R and T_S. Both T_R and T_S are linearly proportional to T_{amb}.

5.4 Effect of Ambient Pressure on Air-Cooling Performance. Figure 10 shows the effects of ambient pressure p_{amb} on T_R, T_S, W_E, and W_I in the case of constant $\dot{V}_E$ and $\dot{V}_I$. Civilian aircraft usually fly at altitudes ranging within 0 m and 13,000 m, so ambient pressures p_{amb} range between 101.3 kPa and 16 kPa based on the ISA. We estimate T_R and T_S in this pressure range at a constant temperature of 15 °C because we first want to know the effect of pressure alone on air-cooling performance.

T_S increases with decreasing p_{amb} because ρ_E decreases and $\dot{m}_E$ decreases at a constant volume flowrate $\dot{V}_E$ of 1.4 m³/s.

T_R increases with decreasing p_{amb}. This is because the density ρ_{IR}, rotating Reynolds number Re_R in Eq. (8), and pipe Nusselt number $Nu_{P,R}$ in Eq. (9) between the rotor and the internal air decrease. This is also because the density ρ_I, pipe Reynolds number $Re_{P,I}$ in Eq. (22), and pipe Nusselt number $Nu_{P,I}$ in Eq. (25) of the internal air passing through the heat exchanger decrease. When p_{amb} values are between 56 kPa and 54 kPa, the flow of the internal air through the rotor is switched from the rotation-dominant flow to the rotation-inertia-affected flow. Thus, $Nu_{P,R}$ is
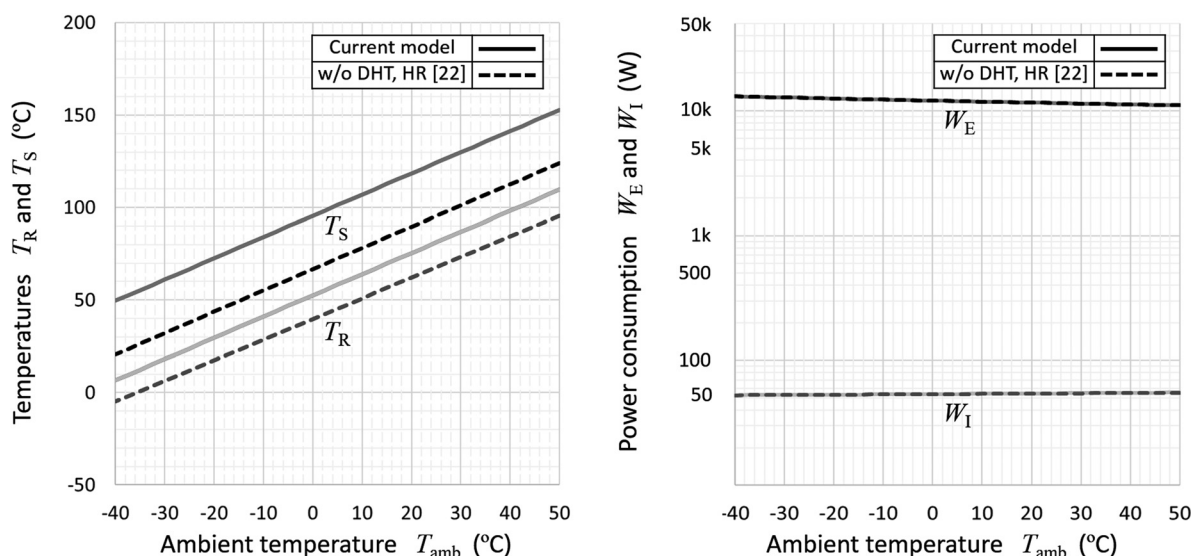

Fig. 9 Permanent magnets and coil temperature, and power consumption with changing ambient temperature estimated by conventional model and current model ($p_{amb} = 101.325$ kPa, $d_R = 150$ mm, $d_A = 100$ mm, $\delta_{TBC} = 0.5$ mm, $\delta_{AIR} = 1$ mm, $a_E = b_E = 10$ mm, $a_I = b_I = 10$ mm, $\dot{V}_E = 1.4$ m³/s, $\dot{V}_I = 0.32$ m³/s)

switched from in Eq. (9) to in Eq. (10), and there is a gap in T_R when p_{amb} values are between 56 kPa and 54 kPa. In addition, when p_{amb} values are between 28 kPa and 26 kPa, the flow of the internal air through the heat exchanger is switched from turbulent flow to laminar flow. Thus, $Nu_{P,I}$ is switched from in Eq. (25) to in Eq. (24), and there is a gap in T_R when p_{amb} values are between 28 kPa and 26 kPa.

Here, we consider the effect of pressure p_{amb} on power consumption W_E. Power consumption W_E is proportional to pressure loss Δp_{lossEH}. From Eq. (46), Δp_{lossEH} is proportional to $\rho_E f_E$. From Eq. (44), f_E is inversely proportional to $Re_{P,E}$ in a laminar flow, and from Eq. (45), f_E is inversely proportional to $Re_{P,E}$ to the power of 1/4 in a turbulent flow. From Eq. (22), $Re_{P,E}$ is proportional to $\dot{m}_E$, and $\dot{m}_E$ is proportional to ρ_E because of the constant volume flowrate $\dot{V}_E$. From air characteristics, the density ρ_E is proportional to p_{amb} under a constant temperature. Consequently, W_E is almost independent of p_{amb} in a laminar flow region, and W_E is almost proportional to p_{amb} to the power of 3/4 in a turbulent flow under a constant volume flowrate $\dot{V}_E$. W_I also has the same tendency.

5.5 Effect of Altitude on Air-Cooling Performance.
During a practical flight, when aircraft fly near ground level, the temperature and pressure are high, while at high altitudes, the temperature and pressure are low. Low temperature is a positive factor, as shown in Fig. 9, and low pressure is a negative factor, as shown in Fig. 10; namely, positive and negative effects arising with increasing altitude cancel each other. Therefore, we elucidated the effects of altitude by using ISA data for temperature and pressure at each altitude. The ISA determines the standard temperature and pressure as follows:

$$T_{amb} = T_{amb,A=0} - 0.0065A$$

$$p_{amb} = p_{amb,A=0}\left[1 - 0.0065\frac{A}{T_{amb,A=0} + 273.15}\right]^{5.2561}$$

$$\text{when } A \leq 11000$$

$$T_{amb} = T_{amb,A=11000} - 71.5$$ (52)

$$p_{amb} = p_{amb,A=11000}\exp\left(-\frac{g[A - 11000]}{RT_{amb,A=11000}}\right)$$

$$\text{otherwise}$$

Figure 11 shows results for T_{Ein} (gray dashed dotted curve), p_{Ein} (dashed double-dotted curve), T_R (light gray curves), T_S (dark gray curves), the power consumption of the internal air flow W_I (light gray curves) and the external air flow W_E (dark gray curves) with changing altitude under conditions based on ISA standard air in the case with a $\dot{V}_E$ of 1.4 m^3/s and a $\dot{V}_I$ of 0.32 m^3/s. T_{amb} decreases by 6.5 °C/1,000 m below $A = 11,000$ m, but T_{amb} becomes constant at -56.5 °C above $A = 11,000$ m. p_{amb} gradually decreases with increasing A.

T_S is affected by both T_{amb} and p_{amb}. The effect of T_{amb} prevails over the effect of p_{amb} until approximately $A = 2,000$ m; thus, T_S gradually decreases. T_S rebounds beyond that point because the effect of p_{amb} gradually prevails over the effect of T_{amb} with increasing A. Above $A = 11,000$ m, only the effect of p_{Eout} operates, and T_S rapidly increases.

T_R also has the same tendency as T_S, although T_R has the minimum value at approximately $A = 6,500$ m. There is a gap in T_R when A values are between 6,250 m and 6,500 m because the flow of the internal air through the rotor is the rotation-dominant flow at A less than 6,250 m, but it is the rotation-inertia-affected flow at A greater than 6,500 m. There is another gap in T_R when A values are between 11,250 m and 11,500 m because the flow of the internal air through the heat exchanger is turbulent at A less than 11,250 m, but it is laminar at A greater than 11,500 m.

Decreasing T_{Ein} increases the external air density ρ_E, and decreasing p_{Ein} decreases ρ_E. With increasing altitude, the pressure effect prevails over the temperature effect; thus, ρ_E, $\dot{m}_E$, and W_E decrease with increasing altitude A at a constant $\dot{V}_E$. As with ρ_E, the internal air density ρ_I, $\dot{m}_I$, and W_I decrease with increasing altitude A for a constant $\dot{V}_I$.

Civilian aircraft usually fly within an altitude range of 0 m to 13,000 m, so the most severe condition is at $A = 13,000$ m in Fig. 11. Although this result does not satisfy the maximum temperature limit of 100 °C for the permanent magnets, it was found that the top-of-climb condition was the most severe, which derives the highest temperatures of permanent magnets and coils.

6 Effect of Air-Cooling Channel Sizes on Air-Cooling Performance for the Top-of-Climb Condition

This section optimizes the sizes of air-cooling channels to reach the minimum value of the sum of power consumption of the external and internal air flows with a setting that keeps permanent magnet temperatures below the maximum temperature limit of 100 °C
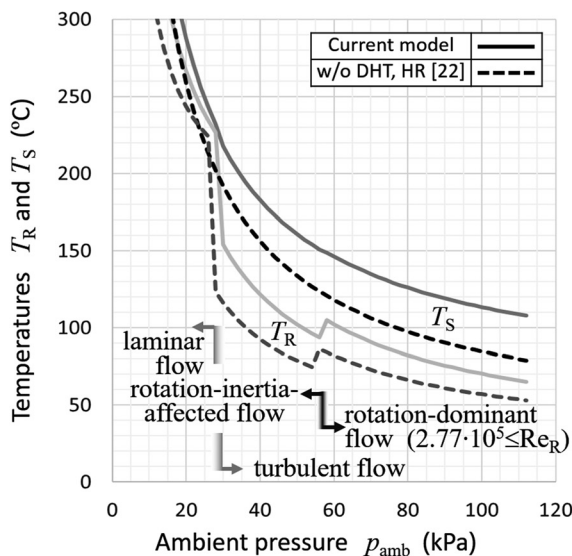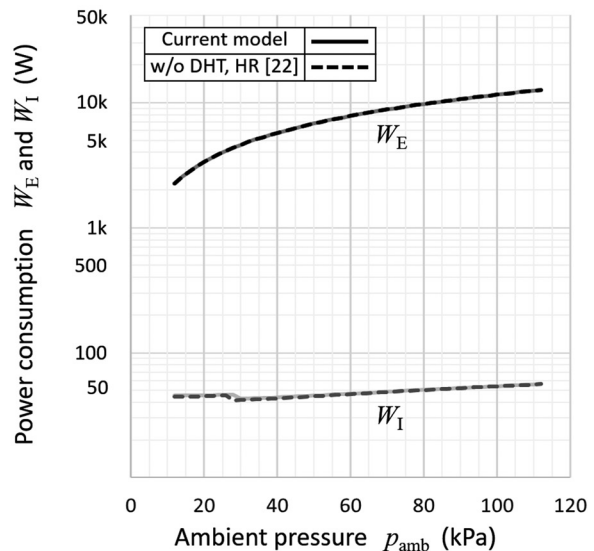

Fig. 10 Permanent magnets and coil temperature, and power consumption with changing ambient pressure estimated by the conventional and current models ($T_{amb} = 15$ °C, $d_R = 150$ mm, $d_A = 100$ mm, $\delta_{TBC} = 0.5$ mm, $\delta_{AIR} = 1$ mm, $a_E = b_E = 10$ mm, $a_I = b_I = 10$ mm, $\dot{V}_E = 1.4$ m^3/s, $\dot{V}_I = 0.32$ m^3/s)
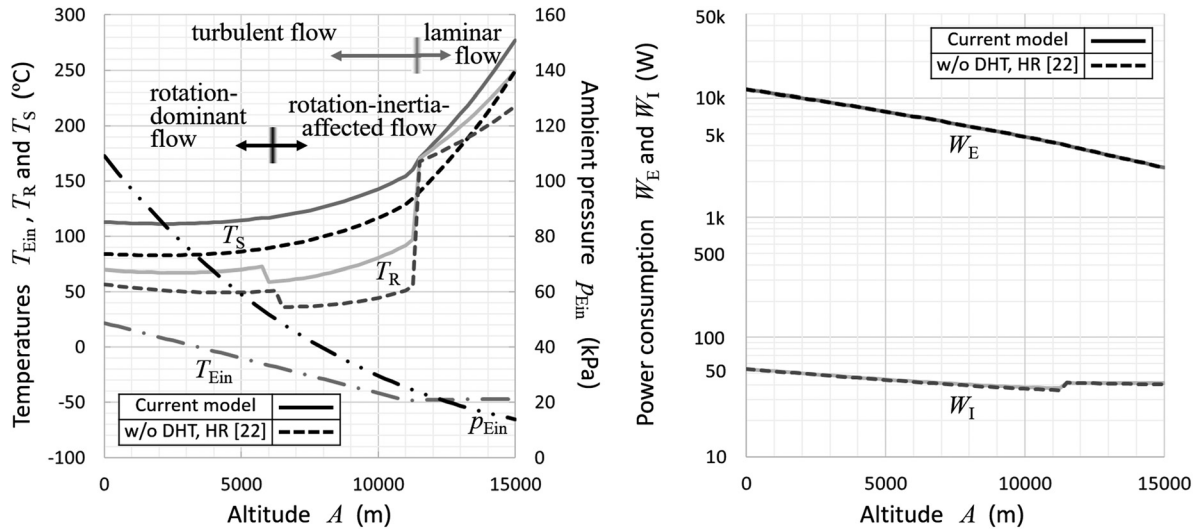
Fig. 11 Temperatures of permanent magnets and coils as well as power consumption with changing altitude estimated by the conventional model and current model (T_{amb} and p_{amb} by ISA, d_R = 150 mm, d_A = 100 mm, δ_{TBC} = 0.5 mm, δ_{AIR} = 1 mm, $a_E = b_E$ = 10 mm, $a_I = b_I$ = 10 mm, $\dot{V}_E$ = 1.4 m^3/s, $\dot{V}_I$ = 0.32 m^3/s)

and coil temperatures below the maximum temperature limit of 250 °C.

6.1 Effect of Clearance Between Rotor and Shaft. As shown in Fig. 4, there is an annular air layer between the inner surface of the rotor and the outer surface of the shaft. Figure 12 shows the coil temperature T_S and permanent magnet temperature T_R as a function of changing rotor inner diameter d_R. There is a gap in T_R when the d_R values are between 0.11 m and 0.1125 m. Decreasing d_R increases the pressure loss through the rotor, increases W_I, increases the inlet temperature of the heat exchanger T_{Iin}, decreases ρ_{Iin}, decreases $\mathrm{Re}_{P,I}$, and switches the internal air flow through the heat exchanger from turbulent to laminar at a d_R of 0.11 m. A much larger d_R (beyond the range of Fig. 12) would switch the internal air flow through the rotor from the rotation-

inertia-affected flow to the rotation-dominant flow, and another gap in T_R would appear.

6.2 Effect of Clearance Between Rotor and Stator. There is an annular air layer in the clearance space between the rotor and stator. The thickness of the annular air layer affects the rate of direct heat transfer between the hotter coils and the colder permanent magnets, and thus, a larger thickness of the annular air layer is preferable for decreasing the direct heat transfer rate in general. On the other hand, a smaller thickness of the annular air layer is preferable for strengthening the electromagnetic force. This paradox may be resolved by applying thermal barrier coatings on the inner surface of the stator and the outer surface of the rotor. Figure 13 shows the effects of the thickness of each thermal barrier coating on the direct heat transfer rate $Q_{S \to R}$, the permanent magnet temperature T_R, and the coil temperature T_S when the total thickness of three layers, the annular air layer and two thermal
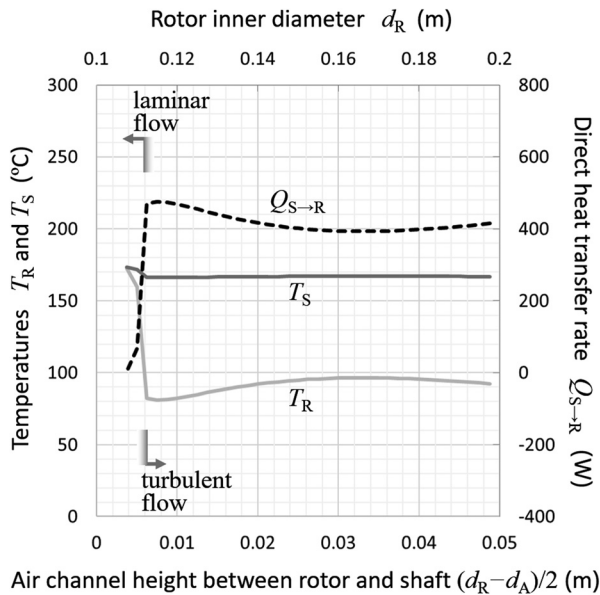
Fig. 12 Effect of rotor inner diameter on temperatures of permanent magnets and coil (T_{amb} = −56.5 °C, p_{amb} = 16.51 kPa, d_A = 100 mm, δ_{TBC} = 0.5 mm, δ_{AIR} = 1 mm, a_E = 7.5 mm, b_E = 14 mm, a_I = 4 mm, b_I = 14 mm, $\dot{V}_E$ = 1.4 m^3/s, $\dot{V}_I$ = 0.32 m^3/s)
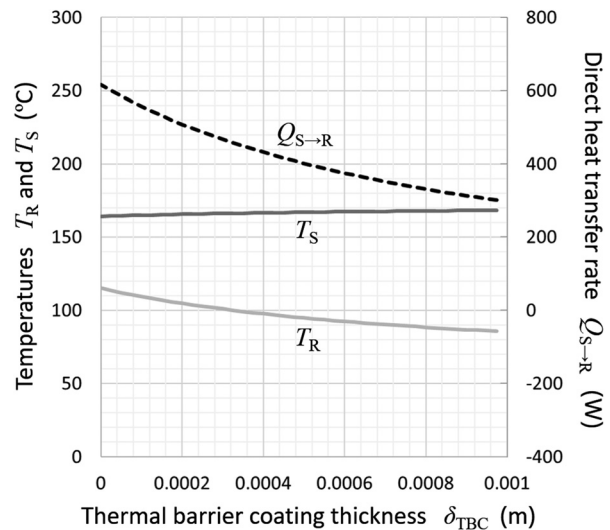
Fig. 13 Effect of the thermal barrier coating thickness on temperatures of permanent magnets and coils as well as the direct heat transfer rate from coils to permanent magnets (T_{amb} = −56.5 °C, p_{amb} = 16.51 kPa, d_R = 150 mm, d_A = 100 mm, δ_{AIR} = 1 mm, a_E = 7.5 mm, b_E = 14 mm, a_I = 4 mm, b_I = 14 mm, $\dot{V}_E$ = 1.4 m^3/s, $\dot{V}_I$ = 0.32 m^3/s)
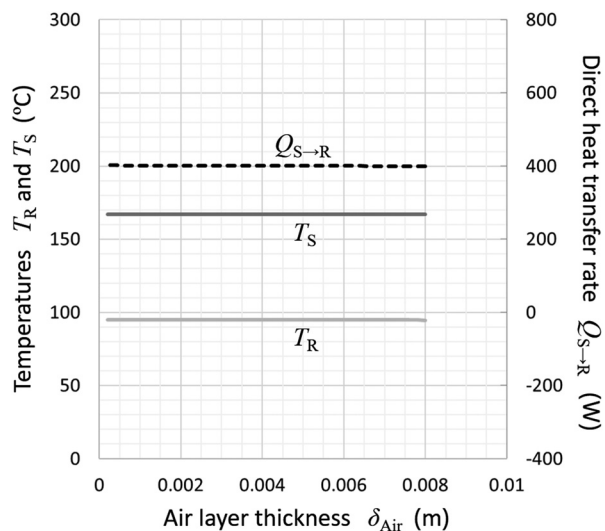
Fig. 14 Effect of the air-layer thickness on temperatures of permanent magnets and coils as well as the direct heat transfer rate from coils to permanent magnets ($T_{amb} = -56.5\,°C$, $p_{amb} = 16.51\,kPa$, $d_R = 150\,mm$, $d_A = 100\,mm$, $\delta_{TBC} = 0.5\,mm$, $a_E = 7.5\,mm$, $b_E = 14\,mm$, $a_I = 4\,mm$, $b_I = 14\,mm$, $\dot{V}_E = 1.4\,m^3/s$, $\dot{V}_I = 0.32\,m^3/s$)

barrier coating layers, is constant. Increasing the thickness of each thermal barrier coating drastically reduces $Q_{S\to R}$ and slightly decreases T_R.

In Fig. 14, the effect of the annular air layer thickness is evaluated for the case with a constant thickness for each thermal barrier coating layer. Changing the thickness of the annular air layer has little effect on $Q_{S\to R}$, T_S and T_R. This is because the heat resistance of the thermal barrier coating layers is much larger than that of the annular air layer; thus, the overall heat transfer coefficient between the coils and permanent magnets $K_{S\to R}$ is almost decided by the values of the heat resistances $\lambda_{TBC,S}/\delta_{TBC,S}$ and $\lambda_{TBC,R}/\delta_{TBC,R}$ in Eq. (4).

6.3 Effect of the External-Air-Channel Height and Width of the Heat Exchanger. Figure 15 shows the coil temperature T_S, the permanent magnet temperature T_R, the power consumption by

the compressors to drive internal air flow W_I and external air flow W_E with changing external-air-channel sizes $a_E = b_E$ and the same volume flow rates $\dot{V}_E = 1.4\,m^3/s$ and $\dot{V}_I = 0.32\,m^3/s$. In this figure, a_E and b_E change together and maintain the same value. In a range of smaller values $a_E = b_E$, decreasing the values of $a_E = b_E$ causes a larger pressure loss because of a faster V_E; thus, W_E increases. At the same time, to compress the external air to resist the larger pressure loss, the external-air inlet temperature of the heat exchanger T_{Ein} is larger due to adiabatic compression at the fan and the external compressor, and thus, it raises T_{Ein} and T_S, resulting in a higher internal-air temperature and a higher T_R. When $a_E = b_E$ is less than 0.004 m, T_{Iin} is sufficiently high, and a high T_{Iin} causes a small density ρ_{Iin} and a small $Re_{P,I}$; thus, the internal flow converts to laminar flow, and there is a gap in T_R when $a_E = b_E$ is 0.004 m. Instead, in a range with larger values of $a_E = b_E$, increasing the values of a_E and b_E results in a higher T_S and T_R because of a smaller Reynolds number $Re_{P,E}$ in Eq. (22); thus, the external air flow removes less heat through the heat exchanger. Therefore, it causes a higher T_S, a higher internal-air temperature, and a higher T_R. Here, the pressure losses of the external air decrease because of a slower V_E in Eq. (46); thus, a smaller W_E is achieved. When $a_E = b_E$ is greater than 0.0185 m, $Re_{P,I}$ is less than 3000; thus, the internal air flow converts to laminar flow. Laminar flow has a much lower heat transfer coefficient with air channels, as shown in Eq. (24); therefore, there is a gap in T_R when $a_E = b_E$ is 0.0185 m. With a smaller T_S, $a_E = b_E = 0.005$ m is the optimum value. With a smaller T_R, $a_E = b_E = 0.0075$ m is the optimum value. With a smaller W_I, $a_E = b_E = 0.008$ m is the optimum value. With a smaller W_E, the largest $a_E = b_E$ is the optimum value. One should choose the more stringent condition among T_S, T_R, W_I, and W_E in considering the overall balance.

Figure 16 shows T_S, T_R, W_I, and W_E with changing an external-air-channel width b_E under various constant values of an external-air-channel height a_E at the volume flow rates $\dot{V}_E = 1.4\,m^3/s$ and $\dot{V}_I = 0.32\,m^3/s$. In the left figure of Fig. 16, T_S (red curves) exhibits the minimum value at an a_E of 0.005 m as in Fig. 15. In a range of a_E less than 0.005 m, a smaller a_E derives a larger T_S because of a larger pressure loss. In a range of a_E greater than 0.005 m, a larger a_E derives a larger T_S because of a smaller $Re_{P,E}$ in Eq. (22). Also, T_R (blue curves) exhibits the minimum value at an a_E of 0.0075 m as in Fig. 15. The tendency of T_R is the same as that of T_S. In the right figure of Fig. 16, a smaller a_E derives a larger W_E because of a larger pressure loss. Instead, W_I is almost
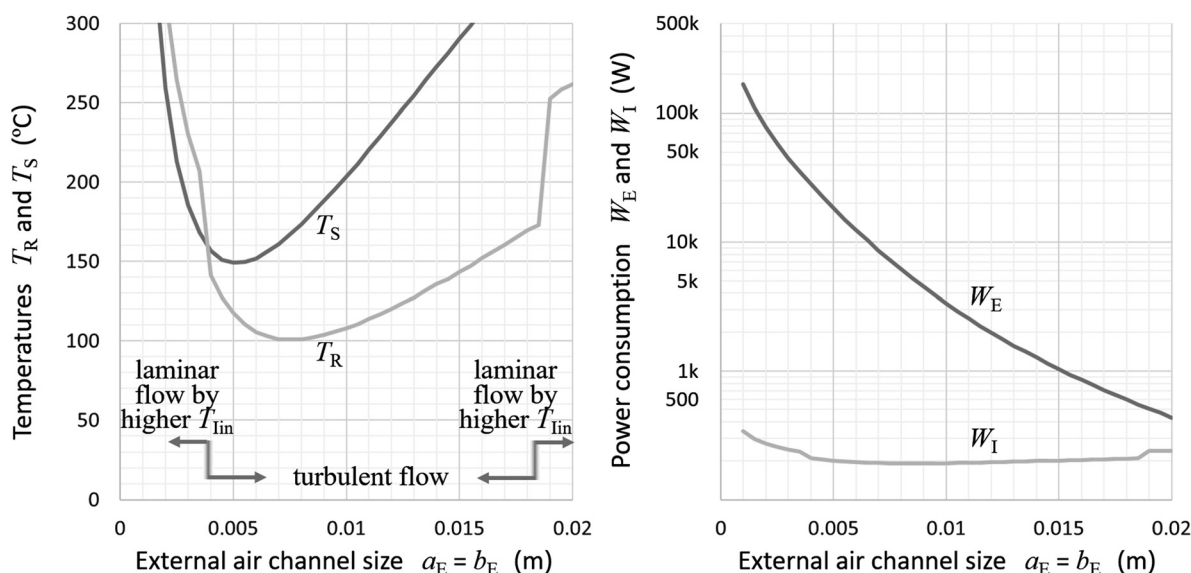

Fig. 15 Effect of channel sizes of external air flow through the heat exchanger on the temperatures of permanent magnets and coil and power consumption ($T_{amb} = -56.5\,°C$, $p_{amb} = 16.51\,kPa$, $d_R = 150\,mm$, $d_A = 100\,mm$, $\delta_{TBC} = 0.5\,mm$, $\delta_{AIR} = 1\,mm$, $a_E = b_E$, $a_I = 4\,mm$, $b_I = 14\,mm$, $\dot{V}_E = 1.4\,m^3/s$, $\dot{V}_I = 0.32\,m^3/s$)
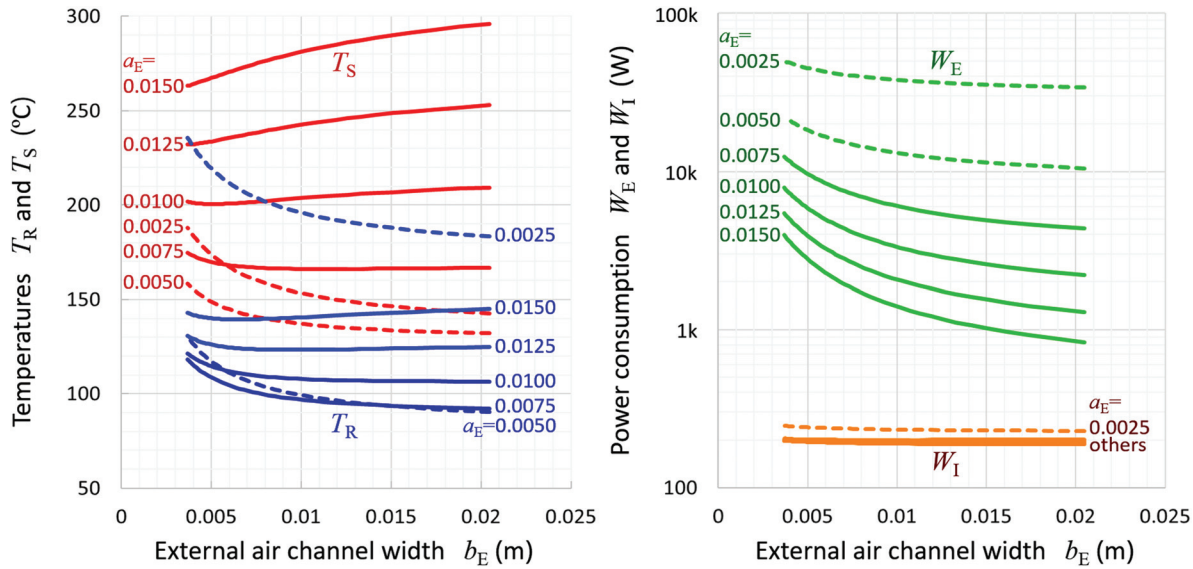
Fig. 16 Effect of channel aspect ratio of external air through heat exchanger on the temperatures of permanent magnets and coil and power consumption ($T_{amb} = -56.5\,°C$, $p_{amb} = 16.51\,kPa$, $d_R = 150\,mm$, $d_A = 100\,mm$, $\delta_{TBC} = 0.5\,mm$, $\delta_{AIR} = 1\,mm$, $a_I = 4\,mm$, $b_I = 14\,mm$, $\dot{V}_E = 1.4\,m^3/s$, $\dot{V}_I = 0.32\,m^3/s$)

independent of a_E because T_R and T_S do not affect W_I in the same manner as in Fig. 9.

6.4 Effect of Internal-Air-Channel Height and Width of the Heat Exchanger. Figure 17 shows T_S, T_R, W_I, and W_E with changing internal-air-channel sizes $a_I = b_I$ at the same volume flow rates $\dot{V}_E = 1.4\,m^3/s$ and $\dot{V}_I = 0.32\,m^3/s$. In this figure, a_I and b_I change together while maintaining the same values. In the left figure of Fig. 17, for a range of smaller values of $a_I = b_I$ less than 0.004 m, decreasing $a_I = b_I$ causes larger pressure loss resulting in a higher temperature of the internal air flow and a higher T_R. In a range of $a_I = b_I$ greater than 0.004 m, larger $a_I = b_I$ derives a larger T_R because of a smaller $Re_{P,I}$ in Eq. (22); thus, the internal air flow radiates less heat through the heat exchanger, and it causes a higher internal-air temperature as well as a higher T_R. In the right figure of Fig. 17, smaller $a_I = b_I$ derives a larger W_I because of a larger pressure loss. Instead, W_E is almost independent of $a_I = b_I$

because T_R and T_S do not affect W_E the same as Fig. 9. With a smaller T_S, $a_I = b_I = 0.0045\,m$ is the optimum value. With a smaller T_R, $a_I = b_I = 0.004\,m$ is the optimum value. With a smaller W_I, the largest $a_I = b_I$ is the optimum value. W_E is constant at any $a_I = b_I$.

Figure 18 shows T_S, T_R, W_I, and W_E with changing an internal-air-channel width b_I under various constant values of an internal-air-channel height a_I at the volume flow rates $\dot{V}_E = 1.4\,m^3/s$ and $\dot{V}_I = 0.32\,m^3/s$. In the left figure of Fig. 18, T_R (blue curves) exhibits the minimum value at a_I of 0.002 m. In a range of a_I less than 0.002 m, a smaller a_I derives a larger T_R because of a larger pressure loss. In a range of a_I greater than 0.004 m, a larger a_I derives a larger T_R because of a smaller $Re_{P,I}$ in Eq. (22). Additionally, there is a gap in T_R due to the transition from turbulent to laminar flow of the internal air in the heat exchanger caused by a smaller $Re_{P,I}$. In the right figure of Fig. 18, a smaller a_I derives a larger W_I because of a larger pressure loss. Instead, W_E is almost
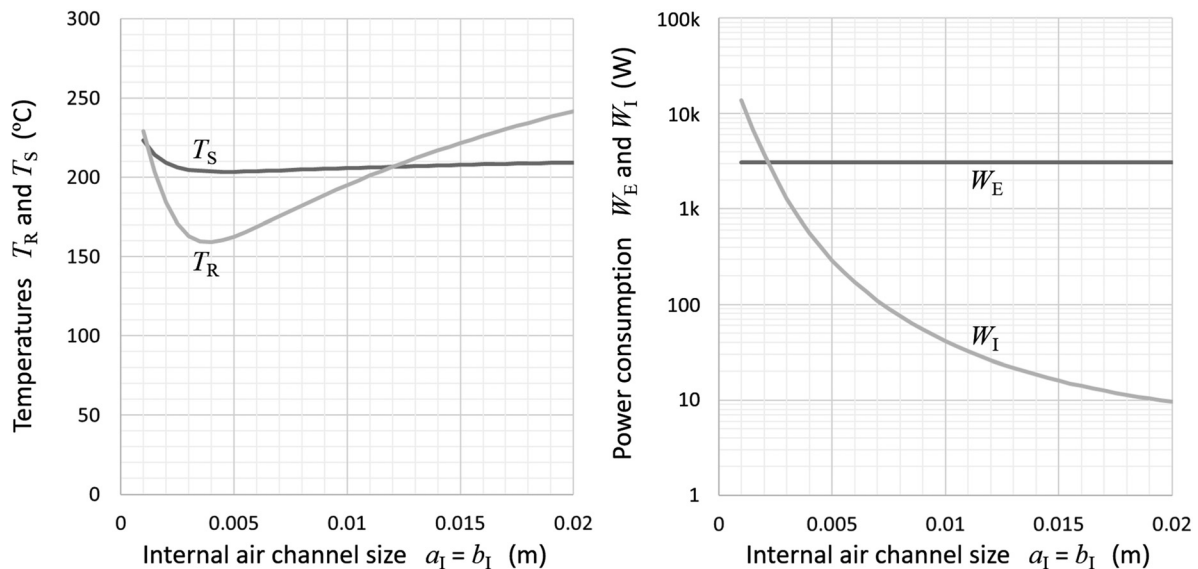

Fig. 17 Effect of channel sizes of internal air through heat exchanger on permanent magnet and coil temperatures and power consumption ($T_{amb} = -56.5\,°C$, $p_{amb} = 16.51\,kPa$, $d_R = 150\,mm$, $d_A = 100\,mm$, $\delta_{TBC} = 0.5\,mm$, $\delta_{AIR} = 1\,mm$, $a_E = 7.5\,mm$, $b_E = 14\,mm$, $a_I = b_I$, $\dot{V}_E = 1.4\,m^3/s$, $\dot{V}_I = 0.32\,m^3/s$)
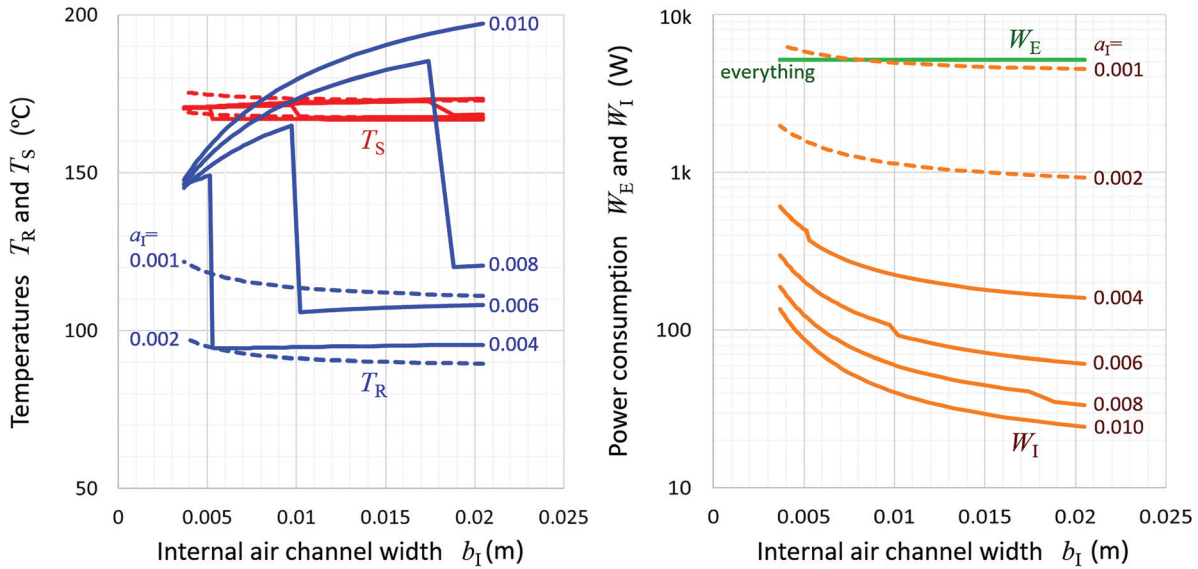
Fig. 18 Effect of the channel aspect ratio of internal air through the heat exchanger on permanent magnet and coil temperatures as well as power consumption ($T_{amb} = -56.5\,°C$, $p_{amb} = 16.51\,kPa$, $d_R = 150\,mm$, $d_A = 100\,mm$, $\delta_{TBC} = 0.5\,mm$, $\delta_{AIR} = 1\,mm$, $a_E = 7.5\,mm$, $b_E = 14\,mm$, $\dot{V}_E = 1.4\,m^3/s$, $\dot{V}_I = 0.32\,m^3/s$)

independent of a_I because T_R and T_S do not affect W_E in the same manner as Fig. 9.

6.5 Air-Cooling Performance at the Optimum Setting. Figure 19 shows the results for T_{Ein}, p_{Ein}, T_R, T_S, W_I, and W_E with changing altitude under conditions based on the ISA standard for air at a $\dot{V}_E$ of $1.4\,m^3/s$ and a $\dot{V}_I$ of $0.32\,m^3/s$ with optimum settings of the air-cooling channel sizes: $d_R = 15\,mm$, $d_A = 10\,mm$, $\delta_{TBC} = 0.5\,mm$, $\delta_{AIR} = 1\,mm$, $a_E = 7.5\,mm$, $b_E = 14\,mm$, $a_I = 4\,mm$, and $b_I = 14\,mm$. The entire tendency seen in Fig. 19 is similar to the results estimated with the current model (by solid curves) shown in Fig. 11, although the air-cooling-channel sizes are optimized in Fig. 19, and the air-cooling-channel sizes are not optimized in Fig. 11. The results shown in Fig. 19 satisfy the maximum temperature limit for the permanent magnets and coils, i.e., T_R should be less than T_{Rlimit} of $100\,°C$ and T_S should be less than T_{Slimit} of $250\,°C$ with the maximum power consumption of $5.35\,kW$ ($W_I = 189\,W$ and $W_E = 5.16\,kW$). The current model

results shown in Fig. 11 do not satisfy the maximum temperature limits, and the maximum power consumption is $3.38\,kW$ ($W_I = 41\,W$ and $W_E = 3.34\,kW$).

Therefore, optimization of air-cooling channel sizes is very important in keeping the temperature limits and minimizing power consumption to enhance the total efficiency of the electric IPM motor. In a practical flight, the required output of the motor at the top-of-climb could be less than that at the takeoff. However, this optimum setting allows pilots to access the maximum output power at the top-of-climb; this constitutes safe redundancy. Of course, the proposed theoretical analysis method is effective at variable outputs and rotation rates along with a practical flight path.

7 Conclusion

In this paper, the effect of altitude on air-cooling performance in an air-cooled 2 MW IPM motor driving an aviation fan was
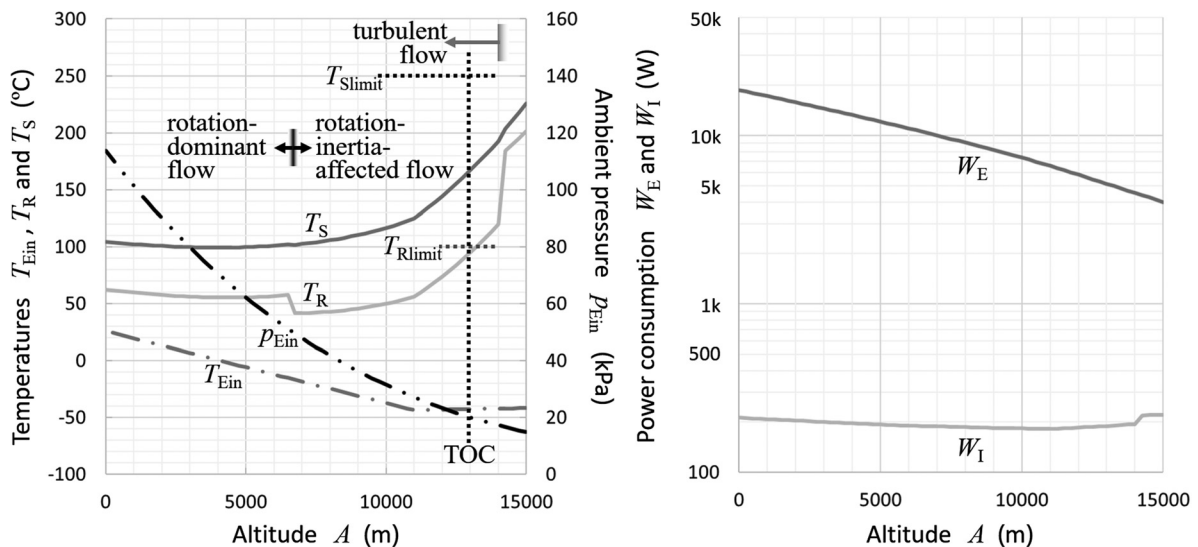

Fig. 19 Permanent magnet and coil temperatures and power consumption with changing altitude at the optimum settings (T_{amb} and p_{amb} by ISA, $d_R = 150\,mm$, $d_A = 100\,mm$, $\delta_{TBC} = 0.5\,mm$, $\delta_{AIR} = 1\,mm$, $a_E = 7.5\,mm$, $b_E = 14\,mm$, $a_I = 4\,mm$, $b_I = 14\,mm$, $\dot{V}_E = 1.4\,m^3/s$, $\dot{V}_I = 0.32\,m^3/s$)

theoretically investigated. Compressor-driven internal air cools permanent magnets (PMs) in a rotor to satisfy the PM maximum temperature limit, and it carries heat from the rotor to the heat exchanger placed outside of a stator. Compressor-driven external air cools coils in the stator via the heat exchanger to satisfy the coil maximum temperature limit, and it carries all heat to the surroundings.

In cases of constant volume flowrates of both airs, with increasing the ambient temperature, the temperatures of the PM and coils linearly increase. The power driving the compressors is almost constant despite the changing ambient temperature. Additionally, with decreasing the ambient pressure, temperatures of the PM and coils rapidly increase because the Reynolds number decreases due to decreasing air density; therefore, the flow mode switches between the rotation-dominant flow and rotation-inertia-affected flow of internal air through the rotor, and the flow mode switches between the laminar flow and turbulent flow of internal air through the heat exchanger. Especially, to satisfy both maximum temperature limits, keeping the turbulent flow mode of internal air through the heat exchanger is necessary. With changing ambient pressure, the power driving the compressor is almost constant in the laminar flow mode of internal air through the heat exchanger, and the power is almost proportional to the ambient pressure to the power of 3/4 in the turbulent flow mode. Furthermore, the effect of altitude on temperatures of the PM and coils was investigated. The most severe condition is the top-of-climb condition. Under this condition, the optimized air-cooling channel sizes satisfy the maximum temperature limits for the PM and coils although the nonoptimized air-cooling channel sizes do not satisfy the maximum temperature limits at the same volume flow rates of internal and external cooling airs.

How and where to switch each flow mode depends on each physical model and correlation used. If each physical model and correlation would be more improved, this approach would derive a more accurate estimation. This approach is very useful for early thermal designs of air-cooled electric motors driving aviation fans.

Acknowledgment

Funding Data

Data Availability Statement

The datasets generated and supporting the findings of this article are obtainable from the corresponding author upon reasonable request.

Nomenclature

a = height of each channel for each air type (m)
b = width of each channel for each air type (m)
c, C = constants
C_P, C_V = isobaric and isochoric specific heats (J/(kg·K))
d = diameter or hydraulic diameter (m)
D = drag force exerted on a flying airplane (N)
E_{pro}, E_{kin} = propulsion energy, kinetic energy (W)

F = thrust generated by the propulsion system (N)
h = heat transfer coefficient (W/(m²·K))
K = overall heat transfer coefficient (W/(m²·K))
ℓ = length of heat exchanger or rotor in the axial direction (m)
m = mass (kg)
$\dot{m}$ = mass flow rate (kg/s)
n = number of channels for each air type
N = number of heat transfer units
Nu_{CL}, Nu_P = clearance Nusselt number, pipe Nusselt number
p = pressure (Pa)
P = peripheral length of each channel for each air type (m)
Pr = Prandtl number
q = heat flux (W/m²)
Q = heat flow rate (W)
$R, \Re$ = gas constant (J/(kg·K)) and universal gas constant (J/(mol·K))
Re_A, Re_P, Re_R = axial, pipe, and rotational Reynolds numbers
S = cross section of each channel for each air type (m²)
t = time (s)
T = temperature (K)
u = average jet velocity from the propulsion system under the main wings (m/s)
U = tangential velocity of the inner surface of the rotor (m/s)
v = flight velocity of an airplane (m/s)
V = axial velocity (m/s)
$\dot{V}$ = volume flow rate (m³/s)
w = local air velocity after a flying airplane (m/s)
W = power consumption (W)
x = position (m)
X = rotation rate in rotations per minute (rpm)
$\alpha, \beta, \gamma, \zeta, \xi,$
$\sigma, \phi, \psi, \theta$ = combined variables
γ = specific heat ratio
δ_B = thickness of the bulkhead (m)
δ_C = diameter difference between coaxial cylinders (m)
$\delta_{TBC,R}, \delta_{TBC,S}$ = thermal barrier coating thickness for the rotor and the stator (m)
ε = ratio of heat capacity flow rates
η_{comp} = compressor efficiency
η_{pro} = propulsion efficiency
λ = thermal conductivity (W/(m·K))
μ = viscosity (Pa·s)
ρ = density (kg/m³)
ω = rotation rate in radians per second (rad/s)

Subscripts

A = shaft
Al = aluminum
B = bulkhead between internal air and external air
E = external air
H = heat exchanger
I = internal air
in = inlet of heat exchanger
L = laterad (outside)
M = medial (inside)
mol = per one mol
out = outlet of heat exchanger
PM = permanent magnet
R = rotor
S = stator
SC = coil in stator
t = time
TBC = thermal barrier coating
x = position from the left end of each heat exchanger or rotor

Function

$$y(x) = y \text{ is a function of } x$$

Appendix A

A1. Radiative Heat Transfer Rate. In an extreme case of a coil temperature $T_S = 250\,°C$, a PM temperature $T_R = 100\,°C$, a temperature at the inner surface of the TBCs on the coil $T_{TBC,S} = 190\,°C$, and a temperature at the outer surface of TBC on the rotor $T_{TBC,R} = 160\,°C$, the radiative heat transfer $Q_{rad,S}$ from the coils and that $Q_{rad,R}$ from the rotor via the annular air layer are as follows, respectively:

$$Q_{rad,S} = \pi[d_{SM} - 2\delta_{TBC,S}]\ell_R \varepsilon_S \sigma_{SB} T_{TBC,S}^4 + [1 - \varepsilon_S]Q_{rad,RL} \quad (A1)$$

$$Q_{rad,RL} = \pi[d_{RL} + 2\delta_{TBC,R}]\ell_R \varepsilon_R \sigma_{SB} T_{TBC,R}^4 + [1 - \varepsilon_R]Q_{rad,S} \quad (A2)$$

where σ_{SB} is Stefan–Boltzmann constant of 5.67×10^{-8} (W/(m^2 K^4)), d_{SM} is the inner diameter of the coils, d_{RL} and ℓ_R are the outer diameter and the length of the rotor, and ε_S and ε_R are emissivities of TBCs on the coils and rotor which are both assumed to be 0.5. Solving the two equations simultaneously

$$Q_{rad,S} - Q_{rad,RL}$$
$$= \pi \ell_R \sigma_{SB} \frac{[d_{SM} - 2\delta_{TBC,S}]T_S^4 - [d_{RL} + 2\delta_{TBC,R}]T_{RL}^4}{1/\varepsilon_S + 1/\varepsilon_R - 1} = 83.3\,W$$
$$(A3)$$

This value is smaller than the direct heat transfer by conduction and convection $Q_{S\rightarrow R}$ by one order of magnitude (refer to Figs. 12–14.)

A2. Validation of the Proposed Method. The proposed theoretical estimation used several models, such as a heat transfer coefficient for each flow scheme in a channel with solid walls, which all were already validated experimentally in the original manuscripts. In addition, a design process for an air-to-air heat exchanger is very common in the thermal engineering field. However, it is important for the proposed theoretical estimation to be validated experimentally or numerically. The authors and colleagues are now preparing validation experiments for the targeted IPM motor with the air cooling designed by the proposed theoretical estimation described in this paper; however, some more time is still needed. Instead, for validation of the proposed theoretical estimation, numerical results of an air-cooled IPM motor with the configuration shown in Table 2 by Jercic et al. [29] were used. They showed the steady-state temperature distribution of PMs and coils as shown in Table 3 when the minimum cooling-air flowrate is 0.096 m³/s at a rotation speed of 1700 rpm.

The heat generation rate should be 3495 W when the power is 118.5 kW and the efficiency is 97.05%. The authors assumed the heat generation rate from the PM is 218.5 W and that from the coils is 3277.25 W. The motor of Jercic et al. has a simple air-cooling scheme different from the authors; therefore, the authors assumed several settings to allow the proposed theoretical estimation to simulate the motor of Jercic et al. First, internal air is always aspirated from the surroundings instead of recirculation; thus, inlet temperatures at both the heat exchanger and the rotor are fixed at 295 K. Second, the authors set the flowrate of the internal air at 0.00177 m³/s to keep the temperature of the PM at 147.6 °C because Jercic et al. did not describe how they cooled the rotor in Ref. [29]. Third, the authors set a heat transfer coefficient at contact surfaces of internal air in the outer heat exchanger at 5 W/(m²·K) to simulate a natural convection cooling by the surrounding air (Table 4).

Table 2 Configuration of IPM motor [29]

Length of rotor and stator	327 mm	Inner dia. of external-air channels	228 mm
Shaft diameter	59 mm	Outer dia. of external-air channels	242.5 mm
Inner dia. of PMs	91 mm	Outer dia. of heat exchanger	262.5 mm
Outer dia. of PM	139 mm	Height of external-air channels	7.5 mm
Inner dia. of coils	142 mm	Width of external-air channels	7.5 mm
Outer dia. of coils	190 mm	Number of external-air channels	36
Inner dia. of heat exchanger	222.5 mm	All values were read and estimated from figures in Ref. [29] by the authors	

Table 3 Operating condition of IPM motor

Power	118.5 kW	Rotation rate	1700 rpm
Efficiency	97.05%	Flowrate of external-air	0.096 m³/s

Table 4 Assumptions for calculation

Heat generation rate from PM	218.5 W	Heat generation rate from coils	3277.25 W
Flowrate of internal air	0.00177 m³/s	Flowrate of external air	0.096 m³/s
Inlet temp. at the heat exchanger of internal air	295 K	Inlet temp. at the heat exchanger of external air	295 K
Inlet temp. at the rotor of internal air	295 K	Heat transfer coefficient on contact surfaces of internal air	5 W/m² K

Table 5 Comparison between Ref. [29] and the proposed theoretical estimation

	Jercic et al. [29]	Proposed theoretical estimation
Temperature of PM	$T_R = 147.6\,°C$	$T_R = 147.6\,°C$
Temperature of coils	116.7 °C, 154.5 °C, 141.2 °C, 141.5 °C, 145.8 °C, 133.6 °C, 154.5 °C, average $T_S = 141.1\,°C$	$T_S = 138.2\,°C$

Using the above assumptions, the proposed theoretical method in this paper estimates the temperature of coils $T_S = 138.2\,°C$ in Table 5. The numerical analysis by Jercic et al. in Fig. 8 in Ref. [29] showed temperatures of the coils at seven points, whose average value was $T_S = 141.1\,°C$

The proposed theoretical method can estimate a reasonable result in the above case, although the authors must validate this theoretical method by some experiments in the near future.

References

[1] Air Transport Action Group, 2021, *Waypoint 2050X Second Edition*, Air Transport Action Group, Geneva, Switzerland.

[2] International Air Transport Association, 2021, *Resolution on the Industry's Commitment to Reach Net Zero Carbon Emissions by 2050*, International Air Transport Association, Montreal, QC, Canada.

[3] Air Transport Action Group, 2021, *Commitment to Fly Net Zero 2050*, Air Transport Action Group, Geneva, Switzerland.

[4] Felder, J. L., 2015, "NASA Electric Propulsion System Studies," National Aeronautics and Space Administration Glenn Research Center, Cleveland, OH, Report No. GRC-E-DAA-TN28410.

[5] Aviation Week and Technology, 2015, *Airbus Looks Toward Light Electric Aircraft Business*, Informa Markets, New York.

[6] Aviation Week and Technology, 2020, *AeroTEC Working With MagniX, Eviation Advance Electric Aircraft*, Informa Markets, New York.

[7] Aviation Week and Technology, 2020, *Flight Experience Makes Pipistrel an Electric Aviation Leader*, Informa Markets, New York.

[8] Dörfler, S., Walus, S., Locke, J., Fotouhi, A., Auger, D. J., Shateri, N., Abendroth, T., Härtel, P., Althues, H., and Kaskel, S., 2021, "Recent Progress and Emerging Application Areas for Lithium–Sulfur Battery Technology," Energy Technol., **9**(1), p. 2000694.

[9] Welstead, J., Felder, J., Guynn, M., Haller, B., Tong, M., Jones, S., Ordaz, I., Quinlan, J., and Mason, B., 2017, "Overview of the NASA STARC-ABL (Rev. B) Advanced Concept," National Aeronautics and Space Administration, Washington, DC, Report No. NF1676 L-26767.

[10] Terao, Y., Ishida, Y., Ohsaki, H., and Oyori, H., 2020, "Electromagnetic Characteristic Comparison of Superconducting Synchronous Motor Characteristics for Electric Aircraft Propulsion Systems," SAE Int. J. Adv. & Curr. Prac. in Mobility, **2**(2), pp. 828–837.

[11] Choi, J., Lee, J. H., Jung, Y. G., and Park, H., 2020, "Enhanced Efficiency of the Brushless Direct Current Motor by Introducing Air Flow for Cooling," Heat Mass Transfer, **56**(6), pp. 1825–1831.

[12] Masson, P. J., Brown, G. V., Soban, D. S., and Luongo, C. A., 2007, "HTS Machines as Enabling Technology for All-Electric Airborne Vehicles," Supercond. Sci. Technol., **20**(8), pp. 748–756.

[13] McCluskey, F. P., Saadon, Y., Yao, Z., and Camacho, A., 2019, "Cooling for Electric Aircraft Motors," 18th IEEE Intersociety Conference on Thermal and Thermomechanical Phenomena in Electronic Systems (ITherm), Las Vegas, NV, May 28–31, pp. 1134–1138.

[14] Wrobel, R., Scholes, B., Hussein, A., Law, R., Mustaffar, A., and Reay, D., 2020, "A Metal Additively Manufactured (MAM) Heat Exchanger for Electric Motor Thermal Control on a High-Altitude Solar Aircraft—Experimental Characterization," Therm. Sci. Eng. Prog., **19**(1), p. 100629.

[15] Liu, F., Hu, J., Li, Y., and Wang, Q., 2020, "Improved Thermal Model of Forced Air-Cooled Motors Considering Heat Transfer in Wire Wound Winding and End Region," IET Electric Power Appl., **14**(6), pp. 943–950.

[16] Malinowski, L., 2003, "Equations for Transient Behavior of Parallel-Flow Multichannel Heat Exchangers," Heat Mass Transfer, **39**(4), pp. 321–325.

[17] Bielski, S., and Malinowski, L., 2005, "An Analytical Method for Determining Transient Temperature Field in a Parallel-Flow Three-Fluid Heat Exchanger," Int. Commun. Heat Mass Transfer, **32**(8), pp. 1034–1044.

[18] Malinowski, L., and Bielski, S., 2009, "Transient Temperature Field in a Parallel-Flow Three-Fluid Heat Exchanger With the Thermal Capacitance of the Walls and the Longitudinal Walls Conduction," Appl. Therm. Eng., **29**(5–6), pp. 877–883.

[19] Chen, J. H., and Malinowski, L., 2014, "Steady State of Three-Fluid Parallel-Flow Heat Exchanger System," J. Eng. Math., **87**(1), pp. 153–165.

[20] Malinowski, L., and Chen, J. H., 2016, "Analytical Solutions of the Equations for the Transient Temperature Field in the Three-Fluid Parallel-Channel Heat Exchanger With Three Thermal Communications," Int. J. Heat Mass Transfer, **96**, pp. 164–170.

[21] Tao, X., Zhou, K., Ivanco, A., Wagner, J. R., Hofmann, H., and Filipi, Z., 2015, "A Hybrid Electric Vehicle Thermal Management System—Nonlinear Controller Design," SAE Paper No. 2015-01-1710.

[22] Ito, Y., Watanabe, T., Seki, N., Oyori, H., and Himeno, T., 2023, "Temperature and Consumed Energy Predictions for Air-Cooled Interior Permanent Magnet (IPM) Motors Driving Aviation Fans—Part 1: Mathematical Analytical Solutions for Incompressible Air Cases," SAE Int. J. Elec. Veh., **12**(1).

[23] Arnold Magnetic Technologies, 2021, *Grain Boundary Diffused Neodymium Iron Boron Magnet Catalog*, Arnold Magnetic Technologies Corporation, Rochester, NY, Rev. 210607.

[24] Taylor, G. I., 1923, "Stability of Viscous Liquid Contained Between Two Rotating Cylinders," Philos. Trans. R. Soc. London, Ser. A, **223**(605–615), pp. 289–343.

[25] Sutherland, W., 1893, "LII. The Viscosity of Gases and Molecular Force," London, Edinburgh, Dublin Philos. Mag. J. Sci., **36**(223), pp. 507–531.

[26] Tachibana, F., and Fukui, S., 1964, "Convective Heat Transfer of the Rotational and Axial Flow Between Two Concentric Cylinders," Bull. Jpn. Soc. Mech. Eng., **7**(26), pp. 385–391.

[27] Seghir-Ouali, S., Saury, D., Harmand, S., Phillipart, O., and Laloy, D., 2006, "Convective Heat Transfer Inside a Rotating Cylinder With an Axial Air Flow," Int. J. Therm. Sci., **45**(12), pp. 1166–1178.

[28] Yamada, Y., and Watanabe, S., 1973, "Frictional Moment and Pressure Drop of the Flow Through Co-Axial Cylinders With an Outer Rotating Cylinder," Bull. Jpn. Soc. Mech. Eng., **16**(93), pp. 551–559.

[29] Jercic, T., Zarko, D., Martinovic, M., Kovacic, M., Juric, J., Hanic, Z., and Stipetic, S., 2017, "Centrifugal Fan Design for Permanent Magnet Synchronous Motor in a Traction Application," 2017 IEEE International Electric Machines and Drives Conference (IEMDC), Miami, FL, May 21–24, pp. 1–7.